Geoscientific
Model Development

Description and evaluation of the tropospheric aerosol scheme in the Integrated Forecasting System (IFS-AER, cycle 47R1) of ECMWF

Samuel Rémy[1], Zak Kipling[2], Vincent Huijnen[3], Johannes Flemming[2], Pierre Nabat[4], Martine Michou[4], Melanie Ades[2], Richard Engelen[2], and Vincent-Henri Peuch[2]

[1]HYGEOS, Lille, France
[2]European Centre for Medium-Range Weather Forecasts, Reading, UK
[3]Royal Netherlands Meteorological Institute, De Bilt, the Netherlands
[4]Météo-France, Toulouse, France

Correspondence: Samuel Rémy (sr@hygeos.com)

Abstract. This article describes the Integrated Forecasting System aerosol scheme (IFS-AER) used operationally in the IFS cycle 47R1, which was operated by the European Centre for Medium Range Weather Forecasts (ECMWF) in the framework of the Copernicus Atmospheric Monitoring Services (CAMS). It represents an update of the Rémy et al. (2019) article, which described cycle 45R1 of IFS-AER in detail. Here, we detail only the parameterisations of sources and sinks that have been updated since cycle 45R1, as well as recent changes in the configuration used operationally within CAMS. Compared to cycle 45R1, a greater integration of aerosol and chemistry has been achieved. Primary aerosol sources have been updated, with the implementation of new dust and sea salt aerosol emission schemes. New dry and wet deposition parameterisations have also been implemented. Sulfate production rates are now provided by the global chemistry component of IFS. This paper aims to describe most of the updates that have been implemented since cycle 45R1, not just the ones that are used operationally in cycle 47R1; components that are not used operationally will be clearly flagged.

Cycle 47R1 of IFS-AER has been evaluated against a wide range of surface and total column observations. The final simulated products, such as particulate matter (PM) and aerosol optical depth (AOD), generally show a significant improvement in skill scores compared to results obtained with cycle 45R1. Similarly, the simulated surface concentration of sulfate, organic matter and sea salt aerosol are improved by cycle 47R1 compared to cycle 45R1. Some biases persist, such as the surface concentrations of nitrate and organic matter being simulated too high. The new wet and dry deposition schemes that have been implemented into cycle 47R1 have a mostly positive impact on simulated AOD, PM and speciated aerosol surface concentration.

1 Introduction

The Copernicus Atmosphere Monitoring Service (CAMS), operated by the European Centre for Medium Range Weather Forecasts (ECMWF) on behalf of the European Commission, has provided operationally near-real-time global analyses and 5 d forecasts of aerosol, trace gases and greenhouse gases twice daily since 2014. It also released the CAMS re-analysis of atmospheric composition (Inness et al., 2019) in September 2018, which has been continually updated since then and now covers 2003 to 2020. These global analyses and forecasts are provided by ECMWF's Integrated Forecasting System (IFS), which combines state-of-the-art meteorological and atmospheric composition modelling together with the data assimilation of satellite products. IFS, with its atmospheric composition extensions, was first developed in the framework of the Global and regional Earth system Monitoring using Satellite and in situ data project (GEMS; 2005 to 2009; Hollingsworth et al., 2008), followed by the Monitoring Atmospheric Composition and Climate series of projects (MACC, MACC-II and MACC-III; 2010 to 2014), and finally CAMS (2014 to present). IFS is originally a numerical

weather prediction system dedicated to operational meteo-
rological forecasts. It was extended to forecast and assimi-
late aerosols (Morcrette et al., 2009; Benedetti et al., 2009;
Rémy et al., 2019), greenhouse gases (Engelen et al., 2009;
Agustí-Panareda et al., 2014), tropospheric reactive trace
gases (Flemming et al., 2009, 2015; Huijnen et al., 2016)
and stratospheric reactive gases (Huijnen et al., 2016). "IFS-
AER" denotes IFS extended with the bin and bulk aerosol
scheme used to provide global aerosol products in the CAMS
project.

The parameterisations of IFS-AER cycle 38R2 and cy-
cle 45R1 have been extensively described in Morcrette et al.
(2009) and Rémy et al. (2019), respectively. Here, we aim
to describe the updates of IFS-AER that have been imple-
mented since cycle 45R1. Most of these updates are used in
the version of cycle 47R1 used for operational forecasts, with
the exception of the new dry and wet deposition schemes,
which were not used operationally in cycle 47R1 for techni-
cal reasons but are now used in operational cycle CY47R3.
A total of 1 year of cycling forecasts with 45R1 and 47R1
IFS-AER have been evaluated against an extensive set of
ground and remote sensing observational datasets. "Cycling
forecasts" refer to experiments that use data assimilation for
the meteorological initial conditions but not for the aerosol
and chemical tracers; 24 h forecasts from the previous cycle
are used as initial conditions for these tracers.

In Sect. 2 we present the main characteristics of IFS-AER,
and its coupling to the operational global chemistry scheme
IFS-CB05 is described. Section 3 details the current and
past operational configurations. Section 4 details the changes
since cycle 45R1 in the representation of primary aerosol
sources. Section 5 presents the upgrade of the aerosol wet
and dry deposition. Finally, Sect. 6 presents simulation re-
sults and budgets and a global and regional evaluation of
cycle 45R1 and 47R1 IFS-AER simulations against remote
sensing products and ground observations.

2   Main characteristics of IFS-AER

IFS-AER is a bulk aerosol scheme with three bins for all
species (except sea salt aerosol and desert dust, for which a
sectional approach is preferred). As such, it is often denoted
as a "bulk–bin" scheme; IFS-AER derives from the Labora-
toire d'Optique Atmosphérique/Laboratoire de Météorologie
Dynamique - Zoom (LOA/LMDZ) model (Boucher et al.,
2002; Reddy et al., 2005) and uses a mass mixing ratio as
the prognostic variable of the aerosol tracers. The aerosol
species and the assumed number size distribution are shown
in Table 1. In contrast to Rémy et al. (2019), only the ni-
trate and ammonium species differ. Since the implementa-
tion of operational cycle 46R1 in July 2019, the prognostic
species are sea salt, desert dust, organic matter (OM), black
carbon (BC), sulfate, nitrate and ammonium. IFS-AER is by
default run coupled with the operational Carbon Bond 2005

(CB05, Yarwood et al., 2005) tropospheric chemistry scheme
that has been integrated into the IFS (Flemming et al., 2015)
and is from here on referred to as "IFS-CB05". IFS-AER can
also be run in stand-alone mode, i.e. without any interaction
with the chemistry, in which case the nitrate and ammonium
species are not included and a specific tracer representing
sulfur dioxide is added, as described in Rémy et al. (2019).

Desert dust is represented with three size bins, with ra-
dius bin limits at 0.03, 0.55, 0.9 and 20 μm). Sea salt aerosol
is also represented with three size bins, with radius bin lim-
its of 0.03, 0.5, 5 and 20 μm at 80 % relative humidity. All
of the sea salt aerosol parameters (concentration, emission,
deposition) are expressed at 80 % relative humidity; this is
in contrast to the other aerosol species in IFS-AER, which
are expressed as dry mixing ratio. The sea salt aerosol mass
mixing ratio, as well as the emissions, burden and sink di-
agnostics, need to be divided by a factor of 4.3 to convert to
dry mass mixing ratio in order to account for the hygroscopic
growth and change in particle density. There is no mass trans-
fer between bins for either dust or sea salt.

The organic matter and black carbon species consist of
their hydrophilic and hydrophobic fractions, with the age-
ing processes transferring mass from the hydrophobic to hy-
drophilic components. Sulfate aerosols (and when not fully
coupled to IFS-CB05, the precursor gas sulfur dioxide) are
represented by one prognostic variable each. When running
fully coupled with IFS-CB05, which has been the operational
configuration since cycle 46R1, sulfur dioxide is represented
in CB05 and thus not in IFS-AER. Since cycle 46R1, two
extra species, nitrate and ammonium, have been included in
the operational products. The nitrate species consists of two
prognostic variables that represent fine nitrate produced by
gas–particle partitioning and coarse nitrate produced by het-
erogeneous reactions of dust and sea salt particles. In all, IFS-
AER is thus composed of 12 prognostic variables when run-
ning stand-alone and 14 when fully coupled with IFS-CB05
(including nitrates and ammonium), which allows for a rela-
tively limited consumption of computing resources.

2.1   Coupling to the chemistry

One of the most important features of cycle 47R1 IFS-AER
is its increasing integration of aerosol and chemistry. The sul-
fur and nitrogen cycles are now represented across IFS-AER
(for particulate species) and IFS-CB05 (for gaseous species),
and IFS-AER provides supplementary input to IFS-CB05 in
order to better represent heterogeneous reactions and the im-
pact of aerosols and photolysis rates.

2.1.1   Sulfur cycle

The simplistic representation of the conversion of sulfur
dioxide into sulfate aerosol used operationally in cycle 45R1
IFS-AER (Rémy et al., 2019) has been replaced by a full
coupling to the chemistry, through which the sulfate produc-

Table 1. Aerosol species and parameters of the number size distribution associated to each aerosol type in IFS-AER (r_{mod} is mode radius, ρ is particle density and σ is geometric standard deviation). Values are for the dry aerosol, with the exception of sea salt, which is given at 80 % RH. The number size distribution is assumed to be monomodal for all species except sea salt and coarse-mode nitrate for which a bimodal size distribution is assumed.

Aerosol type	Size bin limits (sphere radius, μm)	ρ (kg m^{-3})	r_{mod} (μm)	σ
Sea salt (80 % RH)	0.03–0.5 0.5–5.0 5.0–20	1183	0.1992, 1.992	1.9, 2.0
Dust	0.03–0.55 0.55–0.9 0.9–20	2610	0.29	2.0
Black carbon	0.005–0.5	1000	0.0118	2.0
Organic matter	0.005–20	2000	0.021	2.24
Sulfates	0.005–20	1760	0.0355	2.0
Nitrate fine	0.03–0.9	1730	0.0355	2.0
Nitrate coarse	0.9–20	1400	0.199, 1.992	1.9, 2.0
Ammonium	0.005–20	1760	0.0355	2.0

tion rates are computed and provided by IFS-CB05. The sulfur chemistry in IFS-CB05 is as described in Huijnen et al. (2010). In short, in total 111 Tg SO_2 is emitted, which is composed of 97 Tg anthropogenic emissions, 13 Tg volcanic emissions and 1 Tg biomass burning emissions. In addition, 38 Tg dimethyl sulfide (DMS) emissions taken from climatological values are applied, which is then oxidised to form SO_2 (37 Tg) and the rest (5.3 Tg) of the methyl sulfonic acid (MSA). This leads to an annual production of 124 Tg sulfate, both through gas-phase oxidation with OH and aqueous-phase oxidation including reactions with H_2O_2 and O_3.

The coupling with IFS-CB05 impacts most aspects of the simulated sulfur cycle. Table 2 shows the budgets of sulfur dioxide and sulfate aerosols for standalone IFS-AER (CY45R1) and IFS-AER (CY45R1) coupled with IFS-CB05 (CY47R1). The sulfur dioxide sources are slightly different in the standalone configuration: emissions from MAC-City (Granier et al., 2011) are used for the SO_2 tracer included in standalone IFS-AER, while the more recent CAMS_GLOB_ANT (Granier et al., 2019) are used for the sulfur dioxide tracer of IFS-CB05 in the coupled configuration. The different sulfur dioxide emissions explain part of the difference between the budgets and surface concentration plots shown below. The wet deposition of sulfur dioxide is represented in IFS-CB05 and not in the standalone version of IFS-AER, which adds an important sink to the simulated sulfur dioxide. Finally, the chemical conversion rates are globally of the same order of magnitude, but with large regional and vertical differences, leading to a much longer simulated lifetime of sulfur dioxide with cycle 47R1. There are no direct sulfate emissions in IFS-AER.

As shown in Table 2, the global budget of sulfate aerosol differs relatively little between the standalone (CY45R1) and coupled (CY47R1) IFS-AER, taking into account the fact that a new wet deposition routine is available in CY47R1, which will be detailed in Sect. 5.

2.1.2 Nitrate and ammonium

The production scheme of nitrate and ammonium through gas–particle partitioning processes and of nitrate from heterogeneous reactions on dust and sea salt particles is detailed in Rémy et al. (2019) and has been adapted from Hauglustaine et al. (2014), which uses the Equilibrium Simplified Aerosol Model (EQSAM, Metzger et al., 2002) approach. These two parameterisations use meteorological parameters provided by IFS and the gaseous precursors (nitric acid and ammonia) as input. The concentrations of the gaseous precursors are provided by IFS-CB05 and are updated alongside those of the particulate products (nitrate and ammonium) following gas–particle partitioning and heterogeneous reaction processes. The gas–particle partitioning scheme estimates nitrate and ammonium production through the neutralisation of HNO_3 using the NH_3 remaining after neutralisation by sulfuric acid:

$$NH_3 + HNO_3 \leftrightarrow NH_4NO_3. \tag{1}$$

The formation of nitrate from heterogeneous reactions of HNO_3 with calcite (a component of dust aerosol) and sea salt particles is accounted for through the following reactions:
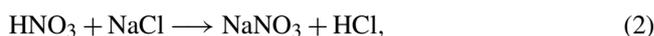
$$HNO_3 + NaCl \longrightarrow NaNO_3 + HCl, \tag{2}$$

Table 2. Global budget for 2017 (annual mean) of SO_2 and SO_2 as simulated by IFS-AER standalone and coupled with IFS-CB05 (fluxes are expressed in $Tg\,S\,yr^{-1}$; burden is expressed in $Tg\,S$).

IFS-AER version	SO_2 emissions	SO_2 chemical loss	SO_2 dry deposition	SO_2 wet deposition	SO_2 burden	lifetime (d)
Stand-alone (CY45R1)	70.3	42.9	27.4	0	0.11	0.57
Coupled (CY47R1)	73.8	41.4	19.9	12.3	0.68	3.36

IFS-AER version	SO_4 emissions	SO_4 chemical production	SO_4 dry deposition	SO_4 wet deposition	SO_4 burden	lifetime (d)
Stand-alone (CY45R1)	0.0	42.9	7.1	35.6	0.357	3.03
Coupled (CY47R1)	0.0	41.4	1.9	39.7	0.367	3.24

$$2HNO_3 + CaCO_3 \longrightarrow Ca(NO_3)_2 + H_2CO_3. \qquad (3)$$

Table 3 shows the budget of the two nitrate species, total particulate nitrate and ammonium, compared with the median values from the AEROCOM phase III experiment (Bian et al., 2017). The comparison to values provided by Bian et al. (2017) can only be qualitative because the emission of the precursor gases (ammonia, nitrous oxides) are different, and the years simulated are also not the same. However, the fact that no major disagreement appears shows that values simulated by IFS-AER fall in the range of values simulated by other models.

2.2 Use of aerosol inputs in IFS-CB05

The global tropospheric chemistry module of IFS, IFS-CB05, uses aerosol mass mixing ratio input from IFS-AER to estimate the reaction rates of heterogeneous reactions on top of aerosol particles. The simulated absorption aerosol optical depth (AAOD) from IFS-AER also intervenes in the computation of photolysis rates Huijnen et al. (2016).

3 Operational configuration

IFS-AER cycle 47R1 was used operationally to provide near-real-time (NRT) aerosol products within CAMS from October 2020 until May 2021, when the new cycle 47R2 became operational. The operational cycle 47R2 does not include any update to IFS-AER; the only feature that impacts simulated aerosol fields besides the upgrade of the meteorological model is the implementation of a maximum value on primary OM emissions, which is meant to compensate for the fact that the emission datasets used underestimate the recent decrease of emissions over China. More details on the implementation of cycle 47R2 can be found at https://confluence.ecmwf.int/display/COPSRV/Implementation+of+IFS+cycle+47r2 (last access: 13 January 2022). The operational cycle 47R2 also runs using single precision instead of double precision for previous operational cycles, which does not impact the output of chemistry and aerosol fields.

In the operational environment, cycle 47R1 IFS-AER assimilates aerosol optical depth (AOD) observations from MODIS collection 6.1 (Levy et al., 2013) and from the Polar Multi Angle Product (Popp et al., 2016). The horizontal and vertical resolution, as well as the time step, are unchanged compared to operational cycle 46R1, with T_L511 (40 km grid cell), 137 levels over the vertical and 900 s. A definition of the vertical levels can be found at https://confluence.ecmwf.int/display/UDOC/L137+model+level+definitions, (last access: 20 January 2022). Prognostic aerosols are used as an input of the IFS radiation scheme to compute the direct radiative effect of aerosols.

Since cycle 46R1, injection heights provided by GFAS (Rémy et al., 2017) have been used for all aerosol and trace gas biomass burning emissions. Since cycle 43R1, as detailed in Rémy et al. (2019), direct anthropogenic SOA emissions scaled on anthropogenic CO emissions have been added to organic matter emissions. This large anthropogenic SOA source derives from the work of Spracklen et al. (2011), who found that they achieved best results in simulating secondary organic aerosols when they assumed a large SOA source (100 Tg per year) from sources that matched anthropogenic pollution. Biogenic SOA emissions that are taken as a 15 % fraction of natural terpene emissions following Dentener et al. (2006) are also added to organic matter emissions. A summary of the operational configurations of the latest versions of the NRT system during the CAMS and MACC projects, as well as the three reanalyses, is shown in Table 4. This table summarises the evolution of IFS-AER since 2013, as well as the changes in the emission datasets used and the horizontal and vertical resolution.

IFS uses a semi-implicit semi-Lagrangian (SL) advection scheme (Hortal, 2002). It is computationally efficient but does not conserve the tracer mass when the flow is convergent or divergent, which is often the case in the presence of orographic features. To compensate for this, mass fixers (MF) have been used for greenhouse gases (Agusti-Panareda et al., 2017), trace gases (Diamantakis and Flemming, 2014) and aerosols in IFS-AER since cycle 43R1.

The operational global CAMS products are routinely evaluated against a variety of observational datasets. The quarterly evaluation reports are available online and can be consulted at https://atmosphere.copernicus.eu/publications (last access: 10 June 2022).

Table 3. The 2017 global budget of nitrate aerosol from gas–particle partitioning and heterogeneous reactions and of ammonium aerosol as simulated by IFS-AER CY47R1 (fluxes are expressed in $\mathrm{Tg\,N\,yr^{-1}}$; burden is expressed in Tg N). The median values from Bian et al. (2017) are indicated in parentheses when they are available and comparable.

Species	Production	Dry deposition	Wet deposition	Burden	Lifetime (d)
Nitrate from gas–particle partitioning	9.1	1.1	8.	0.11	4.21
Nitrate from heterogeneous reactions	14.3	5.3	9.0	0.08	2.04
Total particulate nitrate	23.4 (13.5)	6.4 (3.4)	17. (10.1)	0.19 (0.14)	2.96 (3.78)
Ammonium	14.5 (24.9)	1.1 (4.5)	13.5 (20.4)	0.12 (0.23)	3.02 (3.37)

Table 4. IFS-AER cycles and options used operationally for near-real-time global CAMS products. MF stands for mass fixer, DDEP stands for dry deposition and SCON stands for sulfate conversion. G01 indicates the Ginoux et al. (2001) dust emission scheme, G01bis indicates the Ginoux et al. (2001) dust emission scheme with modified distribution of the emissions into the dust bins and N12 indicates the Nabat et al. (2012) dust emission scheme. M86, G14 and A16 indicate the Monahan et al. (1986), Grythe et al. (2014) and Albert et al. (2016) sea salt aerosol emission schemes, respectively. R05 corresponds to the version of the parameterisation described in Reddy et al. (2005). R05bis is the updated simple sulfate conversion scheme with temperature and relative humidity dependency. CF stands for the wet deposition parameterisation using condensation fluxes (as implemented in cycle 46R1). L19 stands for wet deposition based on Luo et al. (2019). ZH01 and ZH14 stand for the Zhang et al. (2001) and Zhang and He (2014) dry deposition parameterisations, respectively. MACCRA, CAMSiRA and CAMSRA are the MACC Reanalysis (Inness et al., 2013), the CAMS interim Reanalysis (Flemming et al., 2015) and the CAMS Reanalysis (Inness et al., 2019), respectively. For the three reanalyses, the date column refers to when the data were first publicly released.

Model version	Date	Resolution	Emissions				MF	DDEP	WDEP	SCON
			Sea salt	Dust	OM/BC	SO$_2$				
CY37R3	04/2013	T255L60	M86	G01	EDGAR	EDGAR	No	R05	R05	R05
CY40R2	09/2014	T255L60	M86	G01	EDGAR	EDGAR	No	R05	R05	R05
CY41R1	09/2015	T255L60	M86	G01	EDGAR	EDGAR	No	R05	R05	R05
CY41R1	06/2016	T511L60	M86	G01	EDGAR	EDGAR	No	R05	R05	R05
CY43R1	01/2017	T511L60	M86	G01bis	MACCity + SOA	MACCity	Yes	R05	R05	R05
CY43R3	09/2017	T511L60	M86	G01bis	MACCity + SOA	MACCity	Yes	R05	R05	R05bis
CY45R1	06/2018	T511L60	G14	G01bis	MACCity + SOA	MACCity	Yes	ZH01	R05	R05bis
CY46R1	07/2019	T511L137	G14	N12	CAMS_GLOB + SOA	CAMS_GLOB	Yes	ZH01	CF	CB05
CY47R1	10/2020	T511L137	A16	N12	CAMS_GLOB + SOA	CAMS_GLOB	Yes	ZH01	CF	CB05
CY47R2	05/2021	T511L137	A16	N12	CAMS_GLOB + SOA	CAMS_GLOB	Yes	ZH01	CF	CB05
CY47R3	10/2021	T511L137	A16	N12	CAMS_GLOB + SOA	CAMS_GLOB	Yes	ZH14	L19	CB05
MACCRA	2013	T255L60	M86	G01	EDGAR	EDGAR	No	R05	R05	R05
CAMSiRA	2015	T159L60	M86	G01	EDGAR	EDGAR	No	R05	R05	R05
CAMSRA	2018	T255L60	M86	G01bis	MACCity + SOA	MACCity	Yes	R05	R05	R05bis

4 Primary aerosol sources

This section describes the updates in the parameterisations of online aerosol emissions for dust and sea salt aerosol since cycle 45R1.

4.1 Sea salt aerosol

In addition to the M86 (Monahan et al., 1986) and the G14 (Grythe et al., 2014) sea salt aerosol emission schemes, a new sea salt emission scheme "A16" based on Albert et al. (2016) has been developed. It is similar to the M86 scheme in the sense that the oceanic whitecap fraction is first estimated as a prerequisite; in the M86 scheme this is done following the work of Monahan and Muircheartaigh (1980). In the A16 scheme, this is done using a statistical fit between a dataset of 1 year of whitecap fraction estimated from remote sens-

ing observations of ocean surface brightness by radiometers onboard the WindSat satellite at two frequencies, i.e. 10 and 37 GHz (Anguelova and Webster, 2006), 10 m wind speed provided by QuickSCAT, and sea surface temperature (SST) provided by ERA-Interim. The whitecap fraction W is expressed as a function of 10 m wind speed U_{10} and SST by

$$W = a(\mathrm{SST})[U_{10} + b(\mathrm{SST})]^2, \tag{4}$$

where

$$a(\mathrm{SST}) = a_0 + a_1\mathrm{SST} + a_2\mathrm{SST}^2,$$
$$b(\mathrm{SST}) = b_0 + b_1\mathrm{SST}.$$

The $a_{0,1,2}$ and $b_{0,1}$ parameters are given in Albert et al. (2016) for the whitecap fraction estimated with WindSat 10 and 37 GHz brightness temperatures. As the coverage of the retrieved whitecap fraction dataset is very good, the sample

size is very large, which makes the fit quite robust. In the IFS-AER implementation of this scheme, using the fit to white-cap from 37 GHz brightness temperature gave better results, and the $a_{0,1,2}$ and $b_{0,1}$ parameters for this wavelength were chosen.

Using the oceanic whitecap fraction as an input, the production flux of sea salt aerosol is then computed by the following formula from Monahan et al. (1986):

$$\frac{dF}{D_p} = 3.610^5 W D_p^{-3} \left(1 + 0.057 D_p^{1.05}\right) 10^{1.19 \exp(-B^2)}, \quad (5)$$

where

$$B = \frac{0.38 - \log(D_p)}{0.65}, \quad (6)$$

and D_p is the particle diameter.

Table 5 shows the simulated emissions, burdens and lifetimes of the three sea salt bins for the three available emission schemes. The lifetime of sea salt aerosol decreases for larger particles because sedimentation, applied only to bin 3, is an effective sink and because the simulated dry deposition velocity increases with particle size for particles above 1 µm diameter. The emissions of super-coarse sea salt aerosol are much higher with the G14 scheme when compared to the two others. Similar to the M86 scheme, the A16 scheme shows a relatively small increase in emissions with bin size. The lifetime of coarse and super-coarse sea salt bins is the lowest with the A16 scheme. The M86 scheme was used operationally until cycle 43R3. The G14 scheme was used operationally in cycles 45R1 and 46R1, while the new A16 scheme was implemented in operational cycle CY47R1 of IFS-AER. More details about the A16 scheme can be found in Rémy and Anguelova (2021).

4.2 Desert dust

A new dust emission scheme has been implemented since cycle 46R1, which combines the approaches of Marticorena and Bergametti (1995) for the representation of the saltation process and of Kok (2011) for the size distribution of dust at emissions. This new dust scheme was adapted from the scheme implemented in TACTIC (Michou et al., 2015; Nabat et al., 2012).

The emissions of dust particles of a given size D_p through sandblasting occurs if the wind friction velocity u^* is above a threshold value $u_t^*(D_p)$, which is written as follows:

$$u_t^*(D_p) = u_{ts}^*(D_p) f_{eff} f_w, \quad (7)$$

where $u_t^* s(D_p)$ represents an ideal minimum threshold friction velocity and is determined according to the parameterisation of Marticorena and Bergametti (1995) as a function of the Reynolds number Re:

$$u_{ts}^*(D_p) =$$
$$\begin{cases} 0.129 \times K \times [1 - 0.858 \times \exp(-0.0617(Re - 10))] & Re > 10 \\ \frac{0.129 \times K}{(1.928 \times Re^{0.092} - 1)^{0.5}} & Re \le 10 \end{cases}, \quad (8)$$

where the Reynolds number Re is parameterised following Marticorena and Bergametti (1995) as

$$Re = 1331.647 \times D_p^{1.561228} + 0.38194, \quad (9)$$

and

$$K = \sqrt{\frac{2 \times g \times \rho_p \times D_p}{\rho_a} \times \left[1 + \frac{0.006}{\rho_g \times g \times (2 \times D_p)^{2.5}}\right]}, \quad (10)$$

where ρ_p is the dust aggregate density taken as $2.6\,\mathrm{kg\,m^{-3}}$, ρ_a is the surface air density and g the gravitational constant. The term f_{eff} is a correction factor accounting for the effect of surface roughness and is expressed as follows:

$$f_{eff} = 1 - \left[\frac{\ln\left(\frac{z_m}{z_0}\right)}{\ln\left(0.35\left(\frac{10}{z_{0s}}\right)^{0.8}\right)}\right]. \quad (11)$$

Finally, f_w accounts for the effect of soil moisture content on the threshold friction velocity. Following Fecan et al. (1999), it is parameterised as follows:

$$f_w = \begin{cases} [1 + 1.21 \times (w - w')^{0.68}]^{0.5} & \text{for } w > w' \\ 1 & \text{for } w < w' \end{cases}, \quad (12)$$

where w is the surface soil moisture, provided by the IFS surface scheme, and

$$w' = 0.0014 \times (\%\mathrm{clay})^2 + 0.17 \times (\%\mathrm{clay}), \quad (13)$$

where %clay is the fraction of soil that is composed of clay. The information on the clay, silt and sand fraction is provided externally by the Global Soil Dataset for use in Earth system models (GSDE, Shangguan et al., 2014). The horizontal flux of dust from saltation is expressed as follows:

$$G = E_{soil} \times \frac{\rho_a}{g} \times S_{rel} \times (u^*)^3 \times \left(1 - \left(\frac{u_t^*}{u^*}\right)^2\right)$$
$$\times \left(1 + \frac{u_t^*}{u^*}\right), \quad (14)$$

where E_{soil} is the soil "erodibility" and S_{rel} is the ratio of the surface of the dust aggregate of diameter D_p over the sum of the surface of aggregates of all diameters. The soil erodibility can be defined as the soil erosion efficiency of a surface under a given meteorological forcing (Zender et al., 2003). It is also often denoted as "dust source function". Because soil erodibility is hard to estimate, several methods have been tested in dust emission schemes, and one of the most commonly used is the topographic approach from Ginoux et al. (2001), which assumes that the topographic depressions are the largest source of dust. In the operational cycle 47R1, the soil erodibility is provided empirically by a climatological

Table 5. Dry sea salt aerosol emissions, burdens and lifetimes simulated by IFS-AER with the M86, G14 and A16 schemes (emissions are in Tg yr^{-1}, burdens are in Tg and lifetimes are in d).

Process	Bin1 (0.05–0.5 µm)	Bin2 (0.5–5 µm)	Bin3 (5–20 µm)	Total
Emissions (M86)	32.2	2767.2	3363.8	6163.2
Burden (M86)	0.09	3.53	1.43	5.05
Lifetime (M86)	1.0	0.46	0.16	0.29
Emissions (G14)	41.6	1799.5	45 531.6	47 372.7
Burden (G14)	0.14	2.86	22.5	25.5
Lifetime (G14)	1.3	0.58	0.18	0.2
Emissions (A16)	110.3	6595.5	13 657.8	20 363.6
Burden (A16)	0.39	4.46	1.41	6.2
Lifetime (A16)	1.3	0.25	0.04	0.11

Table 6. Desert dust emissions, burdens and lifetimes simulated by IFS-AER with the Ginoux01 (G01) and Nabat12 (N12) schemes (emissions are in Tg yr^{-1}, burdens are in Tg and lifetimes are in d).

Process	Bin1 (0.05–0.55 µm)	Bin2 (0.55–0.9 µm)	Bin3 (0.9–20 µm)	Total
Emissions (G01)	87.9	292	2054.9	2434.8
Burden (G01)	1.7	5.9	8.5	16.1
Lifetime (G01)	7.0	7.2	1.5	2.4
Emissions (N12)	4.9	45.2	3248.5	3298
Burden (N12)	0.12	1.0	13.5	14.6
Lifetime (N12)	8.9	8.1	1.5	1.6

dataset of the frequency of occurrence of dust AOD > 0.4, as provided by Paul Ginoux and introduced in Ginoux et al. (2012). In cycle 46R1, the climatological frequency of dust AOD > 0.2 was used, which led to an overestimation of simulated dust AOD.

The friction velocity u^* is computed using as an input the 10 m wind speed that includes a gustiness effect, computed as in Rémy et al. (2019). Finally, the flux of vertically emitted dust is computed from the horizontal flux using Gilette (1979):

$$H = G \times F_{\text{bare}} \times C \times \begin{cases} 10^{0.134 \times (\%\text{clay}) - 6.0} & \text{for } \%\text{clay} \leq 17\,\% \\ 10^{-0.09 \times (\%\text{clay}) - 2.19} & \text{for } \%\text{clay} > 17\,\% \end{cases}, \quad (15)$$

where F_{bare} is the fraction of the soil that is bare; C is a normalisation constant set to 0.034, similar to the value used in Nabat et al. (2012) who used 0.035. This formula is integrated for all particle diameters D_p and provides the total flux of emitted dust. In order to distribute this flux into the three bins, the size distribution at emissions of Kok (2011) is used, which means a much larger share of emissions being distributed to the super-coarse bin compared to the Ginoux et al. (2001) scheme that was used operationally before cycle 46R1. This is illustrated by Table 6, and as a consequence the simulated lifetime of total dust is significantly lower with the new scheme compared to the old scheme because the super-coarse dust bin has a much shorter lifetime from increased dry deposition and sedimentation.

The 2017 annual total (sum of all bins) dust emissions with the two emission schemes is shown in Fig. 1. There is a much higher regional variability of yearly averaged dust emissions with the new scheme. In addition, dust emissions are higher in the Sahel and many parts of the Sahara and are mostly lower over the Taklamakan and Gobi deserts.

5 Removal processes

In this section, updates to the removal processes compared to the parameterisations implemented in cycle 45R1 of IFS-AER and described in Rémy et al. (2019) are presented.

5.1 Dry deposition

A new parameterisation of aerosol dry deposition following Zhang and He (2014) has been implemented in cycle 47R1 IFS-AER but is not used operationally for technical reasons and is expected to be used in CY47R3. The operational dry deposition scheme still follows the approach of Zhang et al. (2001), as adapted in Rémy et al. (2019). The Zhang and He (2014) has been implemented because it gave good results in a recent intercomparison of dry deposition schemes (Khan and Perlinger, 2017) and because it divides particles into size ranges, i.e. fine, coarse and giant (super-coarse), instead of using the particle size as an input. Only the surface resistance differs compared to the Zhang et al. (2001) scheme. The in-
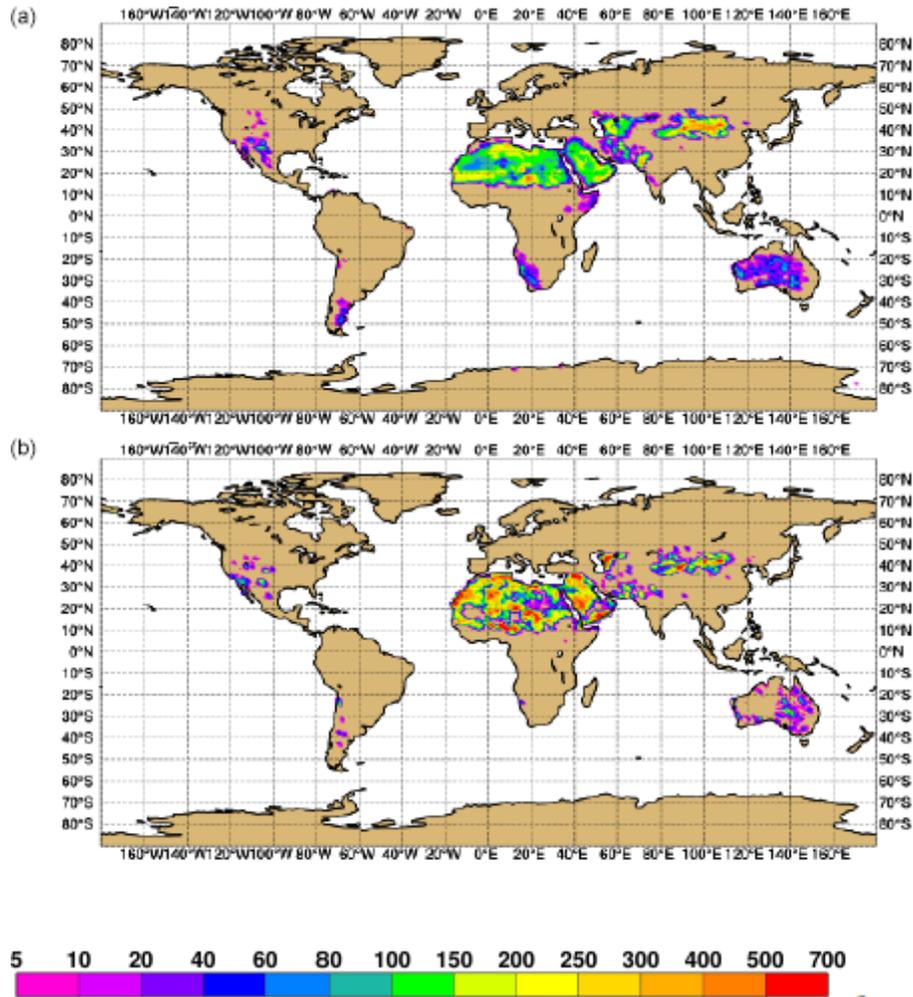
Figure 1. Annual total emissions of dust for 2017 as simulated by CY45R1 and CY47R1 (**b**) (in $g\,m^{-2}\,yr^{-1}$).

verse of the surface resistance is also referred to as surface deposition velocity and denoted as V_s. It is computed as a function of the particle diameter D_p and friction velocity u^* as follows:

$$V_s = \begin{cases} a_1 \times u^* \text{ for } D_p \leq 2.5\,\mu m \\ \left(b_1 \times u^* + b_2 \times u^{*2} + b_3 \times u^{*3}\right) \times \exp\left(K_1 \times \left(\frac{LAI}{LAI_{MAX}} - 1\right)\right) \\ \quad \text{for } 2.5\,\mu m < D_p \leq 10\,\mu m \\ \left(d_1 \times u^* + d_2 \times u^{*2} + d_3 \times u^{*3}\right) \times \exp\left(K_2 \times \left(\frac{LAI}{LAI_{MAX}} - 1\right)\right) \\ \quad \text{for } D_p > 10\,\mu m \end{cases}, \quad (16)$$

where

$$K_1 = c_1 \times u^* + c_2 \times u^{*2} + c_3 \times u^{*3},$$

$$K_2 = e_1 \times u^* + e_2 \times u^{*2} + e_3 \times u^{*3} \times SST,$$

where a_i, b_i, c_i, d_i and e_i are land-surface-dependent coefficients provided by Zhang and He (2014) and LAI_{MAX} is the maximum leaf area index for a give land surface category. Figure 2 shows a comparison of the simulated dry deposition velocity of the two schemes over a particular land surface category (desert).

5.2 Wet deposition

5.2.1 In-cloud scavenging in cycle 46R1

Several updates have been added to the representation of in-cloud scavenging in cycle 46R1. The in-cloud scavenging rate (in s^{-1}) at model level k of an aerosol i is written as follows:

$$W_{i,k}^I = \exp(-\beta_k \times D_i) \times f_k, \quad (17)$$

where D_i is the in-cloud scavenging coefficient, defined as the fraction of the aerosol in the cloudy part of the grid box that is embedded in the cloud liquid and ice water. f_k is the cloud fraction at level k. The value of the parameter D_i is different for water and ice droplets: for water droplets, the values of $D_{i,w}$ from Table 7 are used, which have been derived from Reddy et al. (2005) and Stier et al. (2005). For ice droplets, $D_{i,c}$ is set to 0.06 for all aerosols following Bourgeois and Bey (2011). The final value of D_i is computed from $D_{i,w}$ and $D_{i,c}$ by weighting them with the ice and water cloud
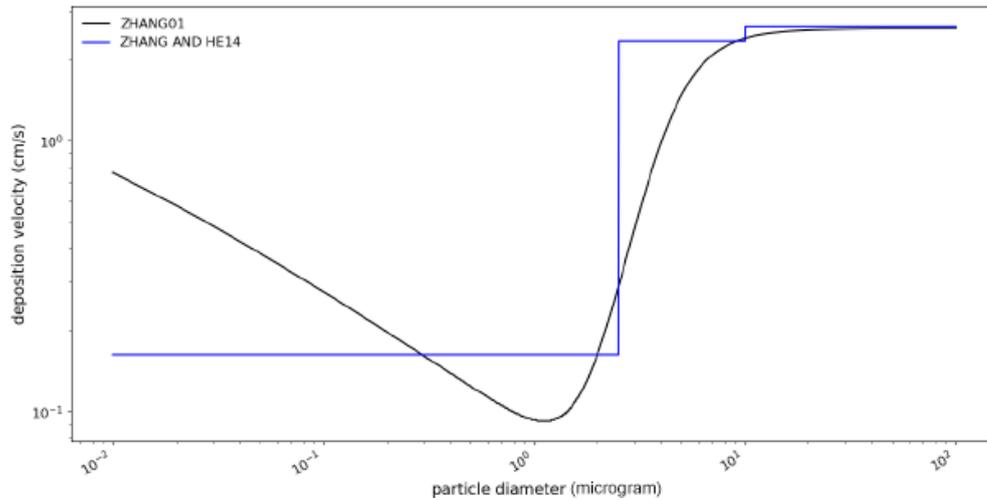
Figure 2. Dry deposition velocity over a desertic surface, as a function of particle size, parameterised by the Zhang et al. (2001) and the Zhang and He (2014) schemes.

Table 7. Value of the parameter D_w, representing the fraction of the aerosol that is embedded in the cloud liquid water.

Species i	$D_{i,w}$ value
Sea salt	0.9
Dust	0.7
OM hydrophilic	0.7
BC hydrophilic	0.7
Sulfate	0.7
Nitrate	0.8
Ammonium	0.9

droplet mass mixing ratio m_c and m_w, respectively:

$$D_i = \frac{m_w \times D_{i,w} + m_c \times D_{i,c}}{m_w + m_c}. \tag{18}$$

β_k is the rate of conversion of cloud water to rain water. Before cycle 46R1, as described in Rémy et al. (2019), β_k was computed following Giorgi and Chameides (1986), β_k, by comparing the precipitation flux at levels k and $k+1$. In cycle 46R1, a new approach has been tested, using the cloud ice and water condensation fluxes instead:

$$\beta_k = (C_{w,k} + C_{c,k}) \times (\rho_k \Delta z_k f_k q_k), \tag{19}$$

where $C_{w,k}$ and $C_{c,k}$ are the cloud ice and water condensation fluxes at level k, q_k is the sum of the liquid and ice mass mixing ratio, ρ_k is the air density at model level k, and Δz_k is the layer thickness of the model level k

The representation of the re-evaporation process has also been made more complex. The release of aerosol particles contained in rain drops at level k occurs if evaporation of precipitation is diagnosed, i.e. if the precipitation flux at level k

is higher than at level $k+1$, where level $k+1$ is below level k. If there is no precipitation at level $k + 1$, then all aerosols that have been subjected to in-cloud scavenging at or above level k are released. If the precipitation flux at level $k + 1$ is not null, the re-evaporation is partial. Before cycle 46R1, it was arbitrarily assumed that half of the scavenged aerosols at or above level k are then released. Since cycle 46R1, a more complex parameterisation has been implemented, following de Bruine et al. (2018). The mass of an aerosol species i that is re-evaporated at level k is computed as a function of the fraction of evaporated precipitation defined with the precipitation flux at level k P_k, $\epsilon_k = \frac{P_{k+1} - P_k}{P_k}$:

$$\delta M_{i,k}^{evap} = \epsilon_k \times \left(\left[1 - \exp^{-2\sqrt{\epsilon_k}} \left(1 + 2 \times \epsilon_k^{\frac{1}{2}} + 2 \times \epsilon_k + \frac{4}{3}\epsilon_k^{\frac{3}{2}} \right) \right] \right.$$
$$\left. \times (1 - \epsilon_k) + \epsilon_k^2 \right) \times \mathrm{Loss}_{scav,i,k} \tag{20}$$

where $\mathrm{Loss}_{scav,i,k}$ is the sum of the mass of aerosol that is subjected to in-cloud wet deposition from level k to the model top.

5.2.2 In-cloud scavenging in cycle 47R1

In cycle 47R1 a new optional formulation of the in-cloud scavenging rate has been implemented that is not yet used operationally for technical reasons but is used in operational cycle 47R3. This formulation is adapted from the approach of Luo et al. (2019). For liquid precipitation,

$$W_{i,k}^I = \frac{P_r}{k \times f_k \times q_{k,r,tot}} \exp^{-k}, \tag{21}$$

where k in s^{-1} is the first-order rainout loss rate Giorgi and Chameides (1986), which represents the conversion of cloud water to precipitation water. $q_{k,r,tot}$ represents the condensed

water content (liquid) within the grid cell. P_r is the rate of new precipitation formation (rain only) in the corresponding grid box. f_k is the cloud fraction at level k. $q_{r,k,tot}$ is derived from the liquid water mass mixing ratio q_k by $q_{k,r,tot} = q_k + \delta_t \times \beta_{r,k}$, where δt is the time step. $\beta_{r,k}$ is defined as in Giorgi and Chameides (1986) using the rain flux at level k $P_{r,k}$:

$$\beta_{r,k} = (P_{r,k+1} - P_{r,k}) \times (\rho_k \Delta z_k). \tag{22}$$

The rainout loss rate is computed as follows:

$$k = D_{i,w} \times \left[K_{min} + \frac{\beta_{k,r}}{q_{k,r,tot}} \right], \tag{23}$$

where $D_{i,w}$ is the fraction of aerosol that is embedded in the cloud liquid or solid water provided by Table 7 and K_{min} is the minimum value of rainout loss rate, set to $0.0001\,\mathrm{s}^{-1}$ in Luo et al. (2019). Finally, the in-cloud scavenging rate in liquid cloud water is expressed as follows:

$$W_{i,k}^{I} = \exp\left(-D_{i,w} \times \left[K_{min} + \frac{\beta_{k,r}}{q_{k,r,tot}} \right] \right)$$
$$\times \frac{f_k \times \beta_{k,r} \times q_{k,r,tot}}{\left(K_{min} + \frac{\beta_{k,r}}{q_{k,r,tot}} \right)}. \tag{24}$$

The formulation of Luo et al. (2019) applies only to liquid precipitation. It has been extended for solid precipitations but taking into account the smaller fraction of aerosols included in solid precipitations; the value of the D_i parameter is divided by 2 for solid precipitation. The scavenging rates for both solid and liquid precipitation are then added.

5.2.3 Below-cloud scavenging in cycle 46R1 and 47R1

Since cycle 46R1, the below cloud scavenging rate is expressed by

$$W_{i,k}^{B} = \mathrm{fp}_k \times \big[(1 - \exp(P_{r,k} \times \alpha_r))$$
$$+ (1 - \exp(P_{i,k} \times \alpha_i)) \big], \tag{25}$$

where $P_{r,k}$ and $P_{i,k}$ are the fluxes of liquid and solid precipitation, respectively, fp_k is the fraction of grid cell at level k in which precipitation occurs, and α_r and α_i are the efficiency with which aerosol variables are washed out by rain and snow, respectively. The values used have been derived from Croft et al. (2009) and are summarised in Table 8.

5.3 Sedimentation

The computation of sedimentation fluxes is unchanged from Rémy et al. (2019) and Morcrette et al. (2009). However, since cycle 47R1 it has been applied to coarse sea salt aerosol in addition to the super-coarse sea salt and dust aerosols. Moreover, the sedimentation velocity is computed dynamically using Stokes's law as a function of particle size and

Table 8. Value of the parameters α_r and α_i.

Species	α_r	α_i
Sea salt fine	0.001	0.005
Sea salt coarse	0.001	0.005
Sea salt super-coarse	0.1	0.005
Dust fine	0.001	0.005
Dust coarse	0.001	0.005
Dust super-coarse	0.1	0.005
OM hydrophilic	0.0001	0.005
OM hydrophobic	0.0001	0.005
BC hydrophilic	0.0001	0.005
BC hydrophobic	0.0001	0.005
Sulfate	0.0001	0.005
Nitrate fine	0.0001	0.005
Nitrate coarse	0.1	0.005
Ammonium	0.0001	0.005

density, which themselves vary as a function of relative humidity for sea salt aerosol:

$$V_s = \frac{2\rho_{p,RH} \times g}{9\mu} r_{p,RH}^2 \times C_F, \tag{26}$$

where $\rho_{p,RH}$ and $r_{p,RH}$ are the particle density and radius, respectively, that depends on relative humidity, g is the gravitational constant, μ is the air viscosity, and C_F is the Cunningham correction factor.

6 Results and evaluation

6.1 Configuration of the IFS-AER simulations

IFS-AER was run in cycling forecast mode without data assimilation from January to December 2017 at a resolution of $T_L 511 L 137$, using emissions and model options similar to the operational CY47R1 run. Simulations have been carried out for cycle 45R1 without coupling to the chemistry and for cycle 47R1 with the operational set of deposition options (denoted "CY47R1"), the wet deposition adapted from Luo et al. (2019) and dry deposition adapted from Zhang and He (2014) (denoted as "CY47R1_NEWDEP"). The two CY47R1 and CY47R1_NEWDEP experiments use IFS-AER coupled to IFS-CB05. In order to assess the model skill independently of resolution and emission inputs, the three simulations, 45R1, 47R1 and 47R1_NEWDEP, used the same horizontal and vertical resolution and the same emission inputs.

6.2 Observations used

A broad range of observational datasets have been used to evaluate the IFS-AER simulations.

6.2.1 In situ

AOD data from the Aerosol Robotic Network (AERONET; Holben et al., 1998) are used to validate IFS-AER forecasts. AERONET level 2 data (cloud screened and quality assured with final calibrations) are used rather than level 1.5. We focus here on AOD at 500 nm. The Maritime Aerosol Network (MAN, Smirnov et al., 2009) component of AERONET provides ship-borne aerosol optical depth measurements from the Microtops II sun photometers. These data provide an alternative to observations from islands and establish validation points for satellite and aerosol transport models. Since 2004, these instruments have been deployed periodically on ships of opportunity and research vessels to monitor aerosol properties over the world's oceans.

PM$_{2.5}$ and PM$_{10}$ observations are provided by the AirNow database (https://www.airnow.gov/about-airnow/, last access: 4 February 2022) over North America, the European Environment Agency (EEA) over Europe and the China National Environmental Monitoring Center over China. For these three regions, special care was taken to use only rural background stations. Observations of speciated aerosol surface concentration from two datasets have been used: the Clean Air Status and Trends Network (CASTNET; https://www.epa.gov/castnet, last access: 20 June 2021) over the US and the European Monitoring and Evaluation Programme (EMEP, https://ebas.nilu.no/, last access: 16 June 2021) over Europe. The CASTNET network is operated by the U.S. Environmental Protection Agency (EPA). The ambient concentrations of gases and particles are collected with an open-face three-stage filter pack at CASTNET sites and a three-stage filter pack or bulk samplers at EMEP sites. The two networks also provide observations of wet deposition of sulfur and nitrogen constituents (both particulate and gaseous). Weekly ambient concentrations of gases and particulate species, including HNO$_3$, SO$_4$, NO$_3$ and NH$_4$, are available from 93 CASTNET sites in 2017. Daily observations of ambient concentration of selected trace gases and aerosol species, including SO$_4$, NO$_3$ and NH$_4$, are available from 37 EMEP stations. In this work, only surface sulfate evaluation is presented.

The Interagency Monitoring of Protected Visual Environment (IMPROVE) programme was initially established in the US as a national visibility network in 1985 and consisted of 30 monitoring sites primarily located in national parks. The network expanded significantly in the late 1990s, and the measurements were diversified to also include some aerosol constituents such as surface concentrations of elemental carbon (or black carbon, BC) and organic carbon (OC) included in PM$_{2.5}$. The use of identical samplers and analysis protocols by the same contractors ensures that data generated by IMPROVE and IMPROVE protocol sites can be treated as directly comparable. The 3-daily data are available from 150 sites in 2017. In this paper we did not use the sites located in mountains in order to avoid possible representativity issues as our model resolution is quite coarse. We used data only from sites that are below 500 m in altitude, which numbered 50 in 2017.

6.2.2 Remote sensing

As described in Sogacheva et al. (2020), a $1° \times 1°$ gridded monthly AOD at 550 nm merged product for the period 1995–2017 was built from 12 individual satellite AOD products retrieved from AVHRR, SeaWiFS, (A)ATSR, MODIS Terra and Aqua, MISR, POLDER, and VIIRS. Different merging approaches were applied, and the resulting AOD was evaluated against AERONET. Optimal agreement of the AOD merged product with AERONET further demonstrates the advantage of merging multiple products. The quality of the merged product is as least as good as that of individual products. The temporal and spatial coverage of the merged product is better than one from the individual products, which makes it a very suitable remote sensing AOD product to compare against simulated AOD at 550 nm.

In order to evaluate the simulated dust AOD at 550 nm, the MODIS Dust AeroSol (MIDAS) dataset was used (Gkikas et al., 2020). MIDAS provides columnar daily dust optical depth (DOD) at 550 nm at a global scale and fine spatial resolution ($0.1° \times 0.1°$) over a 15-year period (2003–2017). This new dataset combines quality-filtered satellite aerosol optical depth (AOD) retrievals from MODIS-Aqua at swath level (collection 6.1, level 2) and DOD-to-AOD ratios provided by the Modern-Era Retrospective analysis for Research and Applications version 2 (MERRA-2, Gelaro et al., 2017) reanalysis to derive DOD on the MODIS native grid.

Observations of dust deposition are relatively sparse. Some are available from a few sites over the Western Mediterranean as described in Vincent et al. (2016) or those collected at the Izaña Global Atmospheric Watch Observatory in the Canary Islands by Waza et al. (2019). An estimate of African dust deposition flux and loss frequency (a ratio of deposition flux to mass loading) along the transatlantic transit is provided by Yu et al. (2019) using the three-dimensional distributions of aerosol retrieved by spaceborne lidar (Cloud–Aerosol Lidar with Orthogonal Polarization, CALIOP) and from AOD products from MODIS, MISR and IASI. Yu et al. (2019) convert the observed AOD into dust mass using assumed values of dust mass extinction efficiency (MEE). Because MEE is strongly dependent on the dust density and particle size distribution (Mahowald et al., 2014), Yu et al. (2019) assume that dust MEE increases linearly with dust transport distance, from $0.37 \, \mathrm{m^2 \, g^{-1}}$ near the African coast (east of $20°$ W) to $0.60 \, \mathrm{m^2 \, g^{-1}}$ at $100°$ W to account for possible preferential removal of larger dust particles during transport. The dust deposition fluxes are then derived from the difference of inbound and outbound dust mass fluxes for each grid cell over the North Atlantic using winds from MERRA-2 and assuming no leak at the top of the atmospheric column. This results in an estimate of seasonal total (dry+wet)

dust deposition over $2° \times 5°$ grid cells in the North Atlantic averaged over 2007–2016.

6.3 Budgets

Budgets are presented in Table 9 for the two cycle 47R1 experiments. For both sea salt and dust, the particle size has an important impact on lifetime: the larger particles have a much shorter lifetime because of more active dry deposition and sedimentation. Compared to results from cycle 45R1 presented in Rémy et al. (2019), the lifetime of fine and coarse dust aerosols are noticeably longer, probably because of changes in wet deposition, which is dominant for these two bins. Similarly, the lifetime of the other fine species, OM, BC and sulfate, are significantly longer than simulated with CY45R1; as wet deposition is the dominant sink for these species, these changes are mainly caused by the updates in wet deposition. For the biomass burning contribution of BC and OM, the use of injection heights for emissions could also contribute: when emitted at surface, biomass burning OM and BC is immediately subjected to dry deposition, which is not the case when it is emitted aloft.

The values indicated in Table 9 can be compared against the values from the AeroCom Phase III control experiment, as reported in Gliß et al. (2021), which also includes data from IFS-AER cycle 46R1. The objective of the AeroCom initiative is to document differences in aerosol component modules of global models and to assemble datasets for model evaluations. A total of 14 global models participated to the Phase III control experiment, which consisted of simulating aerosols for the years 1850 and 2010. All models used the same CMIP6 emissions. The AeroCom median refers to the 2010 experiment. Because the AeroCom experiments are for 2010 and used a different set of emission inputs, the median is not fully comparable to values provided by IFS-AER simulations of the year 2017. However, they give an indication of how IFS-AER broadly compared to other global aerosol models.

For the sum of the emissions of dry sea salt aerosol (i.e. divided by the factor 4.3) for the three bins stands at 21 147 Tg yr^{-1}, which is much higher than the AeroCom median (4980 Tg yr^{-1}) and is the highest of all models reported in Gliß et al. (2021), except for IFS-AER cycle 46R1 at more than 50 000 Tg yr^{-1}, which used the Grythe et al. (2014) sea salt aerosol emission scheme. This value is heavily influenced by the cutoff radius for sea salt aerosol, which at 20 μm at 80 % RH is probably one of the highest. The lifetime of sea salt aerosol is also the lowest of all models for similar reasons: super-coarse sea salt with a very short lifetime is much more abundant than the other sea salt aerosol bins, which show a relatively longer lifetime. Nevertheless, the fact that the lifetime of simulated sea salt aerosol is significantly lower than all other models may be a sign that sinks are too active in IFS. The fact that sea salt aerosol lifetime is increased with the new deposition options also agrees with this conclusion.

For dust, the total emissions are simulated to reach 3297.6 Tg yr^{-1} with IFS-CY47R1, lower than the 5650 Tg yr^{-1} reported in Gliß et al. (2021) with IFS-AER cycle 46R1. This lower value is caused by the update of the dust source function that occurred in cycle 47R1, as mentioned above. The cycle 47R1 emissions are significantly higher than the AeroCom phase III median (1440 Tg yr^{-1}) and are above all other models, as was the case for sea salt aerosols. Similar to the results for sea salt aerosol, this could be because the cutoff radius (20 μm dry radius) is higher than most models. The lifetime of simulated dust stands at 1.5 d with cycle 47R1, which is much lower than the AeroCom phase III median. The most likely explanation is that the bulk of simulated dust with IFS-AER is super-coarse dust, both because of the high cutoff diameter and because the size distribution of emitted dust follows Kok (2011), with more emissions of super-coarse dust relative to other size distributions of dust.

Organic matter emissions are also among the highest reported in Gliß et al. (2021) at 192 Tg yr^{-1}. This probably comes from the SOA components, as relatively few models directly emit SOA as a fraction of organic matter. The lifetime is simulated to be 4.6 d, shorter than the AeroCom phase III median (6 d) but within its bounds, as 4 models out of 13 (excluding IFS-AER cycle 46R1) simulate shorter lifetimes for organic matter. For black carbon, there is a higher level of consensus for the emissions, which are very close between all models. The simulated lifetime, 4.4 d, is slightly lower than the AeroCom median (5.5 d). For both organic matter and black carbon, the new deposition options bring an increase in simulated lifetime, which reduce the difference with the AeroCom median.

Chemical production of sulfate (124 Tg yr^{-1}) is quite close to the AeroCom median (143 Tg). The simulated lifetime (3.2 d) is shorter than the AeroCom median (4.9 d). For nitrate production (103.9 Tg yr^{-1}), the IFS-AER cycle 47R1 value is among the highest and is much higher than the AeroCom median value of 32.5 Tg yr^{-1}. However, the variability between AeroCom models is very high, which is partly explained by the fact that some include nitrate production from heterogeneous reactions of dust and/or sea salt aerosol particles (IFS-AER represents both sources). As for most species, the simulated lifetime of nitrate (3 d) is shorter than the AeroCom median (3.9 d), but the variability is also high for this parameter.

6.4 Simulated AOD at 550 nm and particulate matter (PM)

6.4.1 PM$_{2.5}$ and PM$_{10}$

Figure 3 shows the global PM$_{2.5}$ and PM$_{10}$ simulated by the CY47R1_NEWDEP experiment for 2017. It can be compared to Fig. 11 of Rémy et al. (2019). For PM$_{2.5}$, maximum values of up to 60–70 μg m^{-3} are simulated over parts

Table 9. CY47R1 IFS-AER mean budgets of dry aerosols for 2017 (fluxes are expressed in $Tg\,yr^{-1}$, burdens in Tg and lifetimes in d). Values from the CY47R1_NEWDEP experiments are shown in parentheses.

Species	Source	Dry dep + sedim	Wet dep	Chemical conv	Burden	Lifetime
Fine-mode sea salt	114.2	9.5 (24.9)	104.6 (89.3)	0	0.3 (0.4)	1 (1.3)
Coarse-mode sea salt	6850	5522 (5797)	1328 (1052)	0	4.5 (5.3)	0.24 (0.27)
super-coarse sea salt	14 183	13 691 (13 768)	492 (415)	0	6.1.4 (1.4)	0.04 (0.04)
Fine-mode dust	4.8	1.3 (1.6)	3.5 (3.2)	0	0.12 (0.13)	9.1 (9.9)
Coarse-mode dust	44.8	9.9 (13.8)	34.9 (31)	0	1. (1.)	8.1 (8.1)
Super-coarse-mode dust	3248	2806 (2814)	442 (434)	0	13.5 (14.4)	1.5 (1.6)
Hydrophobic OM	95.9	6.5 (11.2)	8.4 (0.4)	−81 (−84.3)	0.4 (0.4)	1.5
Hydrophilic OM	95.9	17.4 (33.1)	159.5 (147.1)	81 (84.3)	2.5 (2.4)	5.1 (4.9)
Hydrophobic BC	8.4	0.83 (1.01)	0.57 (0.1)	−7 (−7.3)	0.031 (0.032)	1.3
Hydrophilic BC	2.1	1(1.5)	8.5 (7.9)	7 (7.3)	0.13 (0.15)	5.2 (5.8)
Sulfate	0	5.7 (14.9)	118.7 (109.5)	124.4 (124.4)	1.1 (1.2)	3.2 (3.5)
Nitrate from gas–particle partitioning	0	4.6 (7.6)	35.9 (27.3)	40.5 (34.9)	0.47 (0.44)	4.2 (4.6)
Nitrate from heterogeneous reactions	0	23.8 (19.9)	39.6 (47.7)	63.4 (67.6)	0.35 (0.48)	2.1 (2.6)
Ammonium	0	1.4 (2.4)	17.5 (15.2)	18.9 (17.6)	0.15 (0.14)	2.9 (2.9)
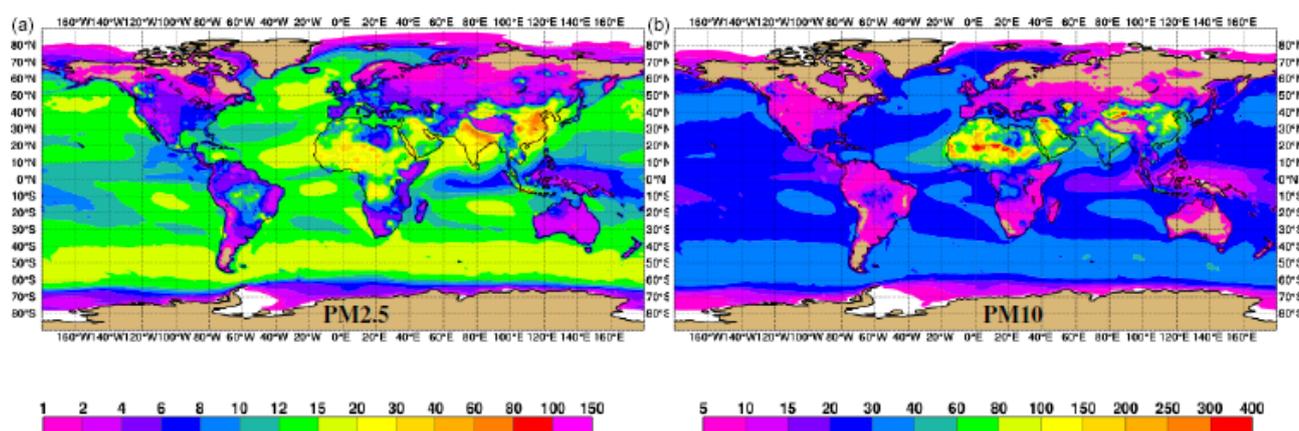
Figure 3. Global mean 2017 $PM_{2.5}$ **(a)** and PM_{10} **(b)** (in $\mu g\,m^{-3}$) simulated by the CY47R1_NEWDEP experiment in cycling forecast mode. Please note the different scales for $PM_{2.5}$ and PM_{10}.

of China and India, mostly from anthropogenic aerosols, and over parts of the Sahara, mostly from desert dust. Over oceans, the mean values vary between 8 and $20\,\mu g\,m^{-3}$. Over Europe and the eastern US, the simulated values vary between 6 and $12\,\mu g\,m^{-3}$. Areas of seasonal biomass burning such as equatorial Africa, parts of Brazil and Indonesia show simulated $PM_{2.5}$ between 10 and $20\,\mu g\,m^{-3}$ on a yearly average. Individual large fire events, such as the "British Columbia" fire of August 2017 also appear over western Canada, lifting the yearly average there to $10–15\,\mu g\,m^{-3}$.

Dust and sea salt aerosols are much more prominent in Fig. 3b. Over oceans, the simulated PM_{10} varies between 20 and $35\,\mu g\,m^{-3}$, while yearly values can reach up to $200–300\,\mu g\,m^{-3}$ over the dust-producing regions of the Sahara, Arabian Peninsula and the Taklamakan desert. PM_{10} over the heavily polluted areas of India and China reaches $80–100\,\mu g\,m^{-3}$, which is only $20–30\,\mu g\,m^{-3}$ more than $PM_{2.5}$ over these regions, which are impacted mainly by fine par-

ticles. Similarly, the simulated PM_{10} values over Europe, US and the seasonal biomass burning regions are $20\%–30\%$ higher than the $PM_{2.5}$ values.

6.4.2 AOD at 550 nm

Figure 4 shows total and speciated AOD at 550 nm simulated by the CY47R1_NEWDEP experiment for 2017. The highest values can be found in the heavily populated regions of the Indian subcontinent and eastern China; the dust-producing regions of the Sahara, the Arabian Peninsula, and the Taklamakan desert; and in the seasonal biomass burning region of equatorial Africa. The transport of dust produced in the western Sahara and over the Taklamakan and Gobi deserts over the Atlantic and Pacific, respectively, are prominent features that can be used to assess the deposition processes. Sea salt AOD is quite evenly spread between the mid-latitude regions, where mean winds are high, and the tropics, where
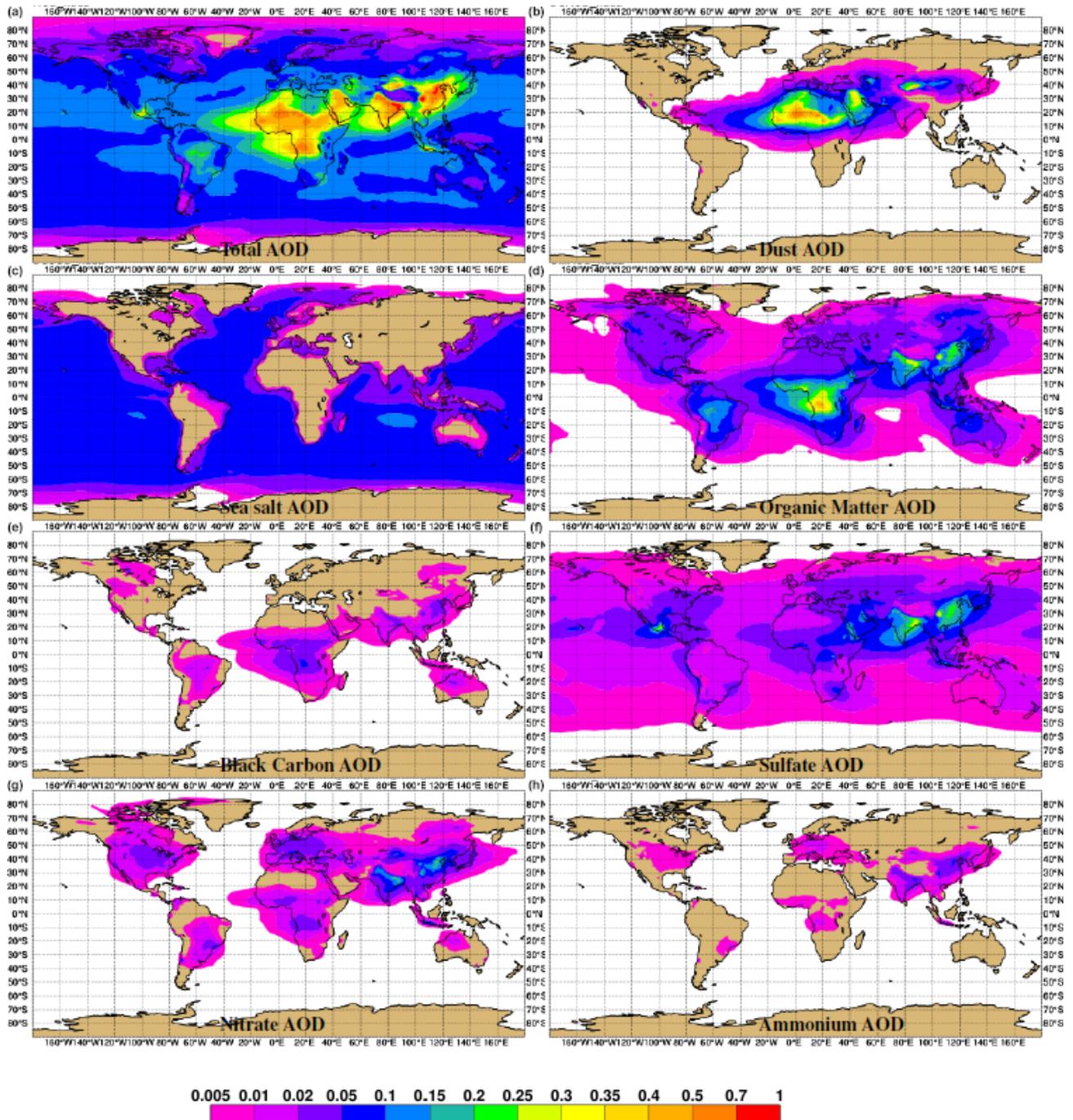
Figure 4. Mean 2017 total **(a)**, dust **(b)**, sea salt **(c)**, OM **(d)**, BC **(e)**, sulfate **(f)**, nitrate **(g)** and ammonium **(h)** AOD at 550 nm simulated by the CY471_NEWDEP experiment.

trade winds are on average less intense but have a relatively more active sea salt production thanks to the dependency of sea salt production on SST. OM is a species that combines anthropogenic and biomass burning sources: AOD is highest over parts of China and India, mostly from secondary organics scaled on anthropogenic CO emissions, and over equatorial Africa, from biomass burning. BC sources are also a combination of anthropogenic and biomass burning origin, the patterns are close to what is simulated for OM. Sulfate AOD is concentrated over heavily populated areas, and a few outgassing volcanoes such as Popocatépetl in Mexico and Kīlauea in Hawaii. Oceanic DMS sources bring a "background" of sulfate AOD over most oceans. Nitrate AOD is highest over the regions where anthropogenic emissions of

Table 10. Average over 2017 of the modified normalised mean bias (MNMB)/fractional gross error (FGE) of simulated daily AOD at 500 nm. $PM_{2.5}$ and PM_{10}. AOD observations are from AERONET level 2. European PM observations are from 65 $PM_{2.5}$ and 138 PM_{10} background rural airbase stations. North American PM observations are from 125 $PM_{2.5}$ stations and 25 PM_{10} background rural stations. Chinese PM observations are from 152 $PM_{2.5}$ background rural stations.

Experiment	Global	Europe	N. America	S. America	Africa	China
AOD CY45R1	−0.25/0.60	−0.55/0.67	−0.33/0.58	−0.34/0.54	−0.03/0.46	0.12/0.56
AOD CY47R1	−0.20/0.49	−0.19/0.40	0.03/0.46	−0.32/0.53	−0.12/0.41	−0.01/0.48
AOD CY47R1_NEWDEP	−0.16/0.48	−0.18/0.39	−0.04/0.46	−0.19/0.46	−0.05/0.39	0.01/0.47
$PM_{2.5}$ CY45R1	–	−0.17/0.53	−0.05/0.55	–	–	0.52/0.69
$PM_{2.5}$ CY47R1	–	−0.05/0.48	−0.09/0.52	–	–	0.21/0.53
$PM_{2.5}$ CY47R1_NEWDEP	–	−0.01/0.46	−0.12/0.48	–	–	0.16/0.51
PM_{10} CY45R1	–	−0.35/0.56	−0.38/0.67	–	–	0.38/0.63
PM_{10} CY47R1	–	−0.18/0.46	−0.36/0.62	–	–	0.15/0.55
PM_{10} CY47R1_NEWDEP	–	−0.13/0.44	−0.41/0.62	–	–	0.12/0.54
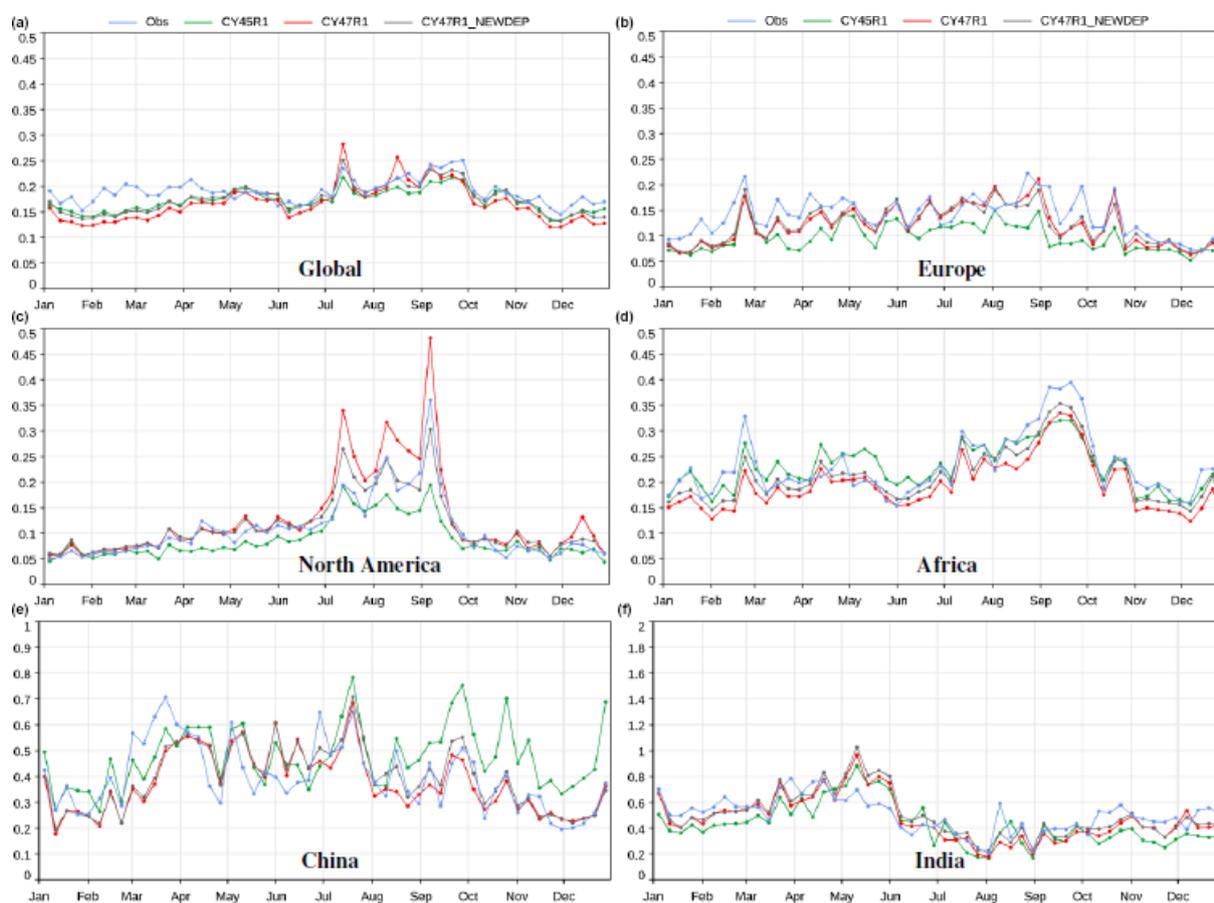
Figure 5. Global **(a)** and regional **(b)**–**(f)** simulated vs. observed level 2 weekly AOD at 500 nm from AERONET averaged over 7 d.

nitrogen oxides are highest, i.e. over India and China. Some secondary maxima also appear over seasonal biomass burning regions from biomass burning emissions of nitrogen oxides. Finally, the features of ammonium AOD are close to those of nitrate AOD but with lower values.

6.5 Evaluation summary

Table 10 shows a summary of global and regional skill scores for AOD at 500 nm and PM for a year of simulation of the CY45R1, CY47R1 and CY47R1_NEWDEP experiments. The modified normalised mean bias (MNMB) and fractional gross error (FGE) are shown so that the metrics
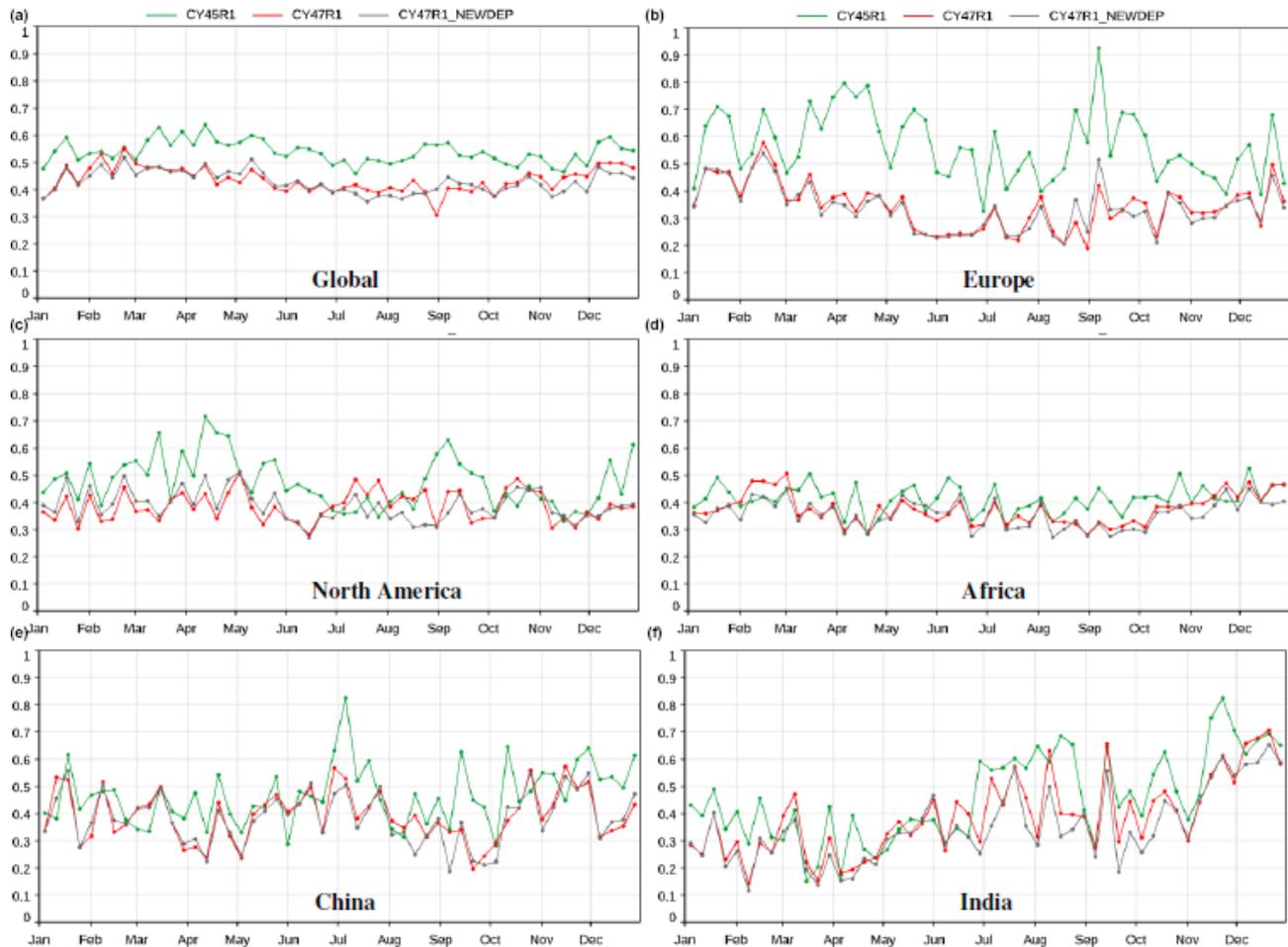
Figure 6. Fractional gross error (FGE) of simulated weekly AOD at 500 nm against global **(a)** and regional **(b)**–**(f)** level 2 AOD from AERONET.

are not too impacted by a few local extreme events, as can be the case with bias and root-mean-square error (RMSE). MNMB varies between -2 and 2; it is defined for a population of N forecasts f_i and observations o_i by the following equation:

$$\text{MNMB} = \frac{2}{N} \sum_i \frac{f_i - o_i}{f_i + o_i}. \tag{27}$$

FGE varies between 0 (best) and 2 (worst) and is defined as follows:

$$\text{FGE} = \frac{2}{N} \sum_i \left| \frac{f_i - o_i}{f_i + o_i} \right|. \tag{28}$$

The AOD at 500 nm as simulated by CY45R1 shows a negative MNMB globally and over all regions except China, ranging from -0.03 over Africa to -0.55 over Europe. The FGE is above 0.5 for all regions except Africa. CY47R1 clearly improves the MNMB: the negative values are reduced everywhere except Africa and range from -0.12 over Africa to -0.32 over South America. FGE is below 0.5 for

all regions except South America. The new deposition options of CY47R1_NEWDEP bring a further improvement to the MNMB, which measured between 0.01 over China and -0.19 over South America. FGE is also improved marginally by NCY47R1_NEWDEP compared to CY47R1: it is reduced by 0.01–0.02 over all regions except South America where the improvement is more noticeable (0.07).

The PM$_{2.5}$ evaluation has only been carried out over Europe, North America and China using only background rural stations.

PM$_{10}$, similar to PM$_{2.5}$, shows a significant improvement in MNMB and FGE over Europe and China and a lower improvement over the US.

6.6 Evaluation against AERONET

Figures 5 and 6 show two measures of skill of the simulated weekly AOD at 500 nm against global and regional AERONET observations: bias and fractional gross error (FGE). There is generally a global negative bias of simulated AOD against AERONET values on the order of 0.02–
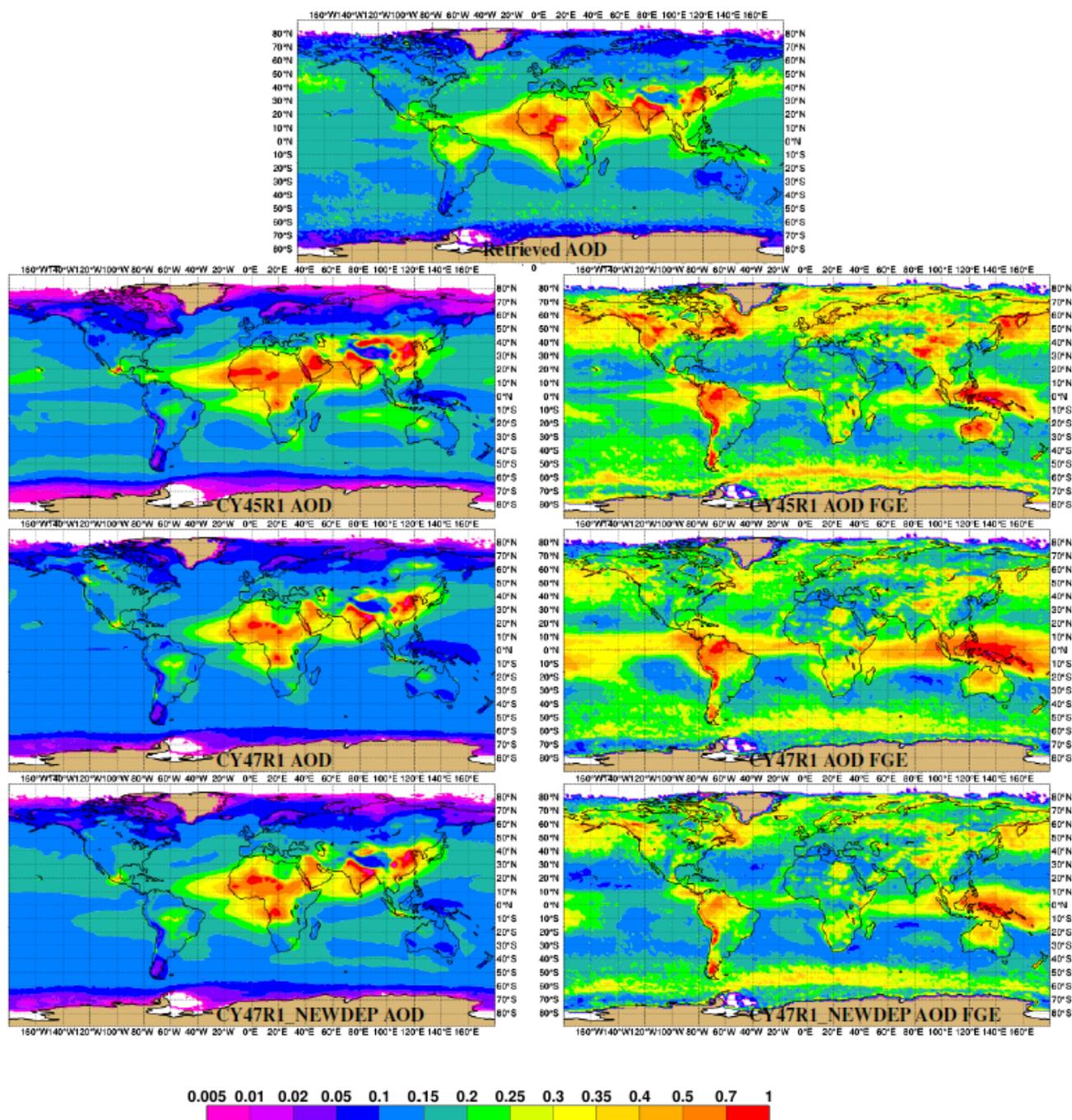
Figure 7. The top panel shows the 2017 average of merged AOD at 550 nm from Sogacheva et al. (2020). The left column shows the co-located simulated yearly AOD for CY45R1, CY47R1 and CY47R1_NEWDEP from top to bottom. The right column shows the fractional gross error of simulated AOD against the merged AOD product for CY45R1, CY47R1 and CY47R1_NEWDEP from top to bottom.

0.03 with CY45R1. This negative bias is slightly worsened by CY47R1 and slightly improved by CY47R1_NEWDEP. The FGE is generally improved by the two CY47R1 experiments. In July and August 2017, large fires in the US and Canada provoked spikes in simulated and observed AOD (consisting mainly of organic matter AOD). The FGE is not impacted, but the RMSE (not shown) is very high during

these 2 months over North America. The regional skill scores against AERONET are more varied. Over Europe, a 0.05 negative bias with CY45R1 is significantly improved with the two CY47R1 experiments (0.02 negative bias) and associated with a reduced FGE, which is generally between 0.5–0.7 with CY45R1 and below 0.5 with the two CY47R1 experiments. Several factors can explain this improvement;
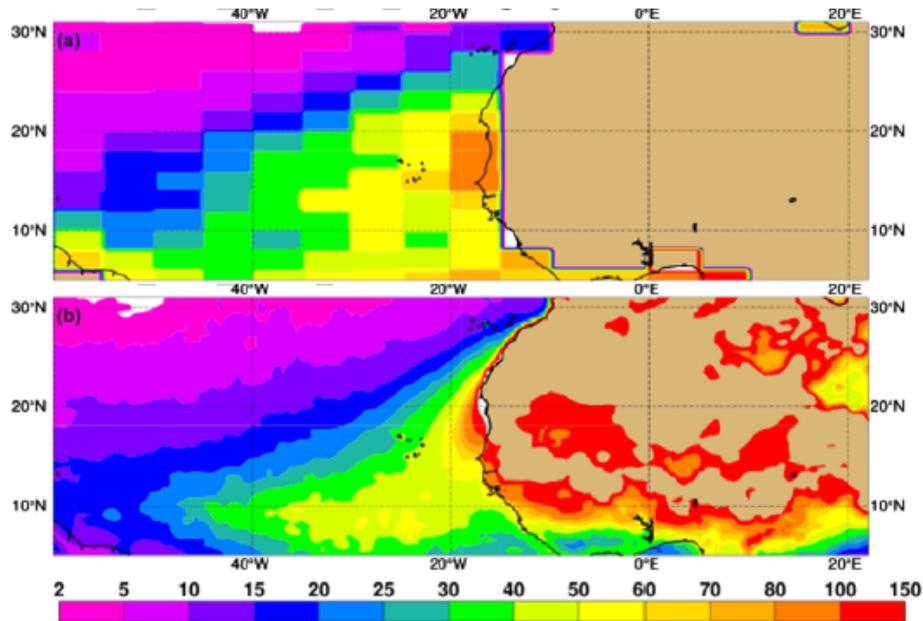
Figure 8. (a) The 2007–2016 mean dust total deposition (in $\mathrm{mg\,m^{-2}\,d^{-1}}$) as estimated by MODIS. **(b)** The mean 2017–2019 dust total deposition as simulated by IFS-AER cycle 47R1 without data assimilation (in $\mathrm{mg\,m^{-2}\,d^{-1}}$).

the dominant cause is probably the presence of nitrate/ammonium aerosols in the CY47R1 experiments. Over North America, the simulated negative bias with CY45R1 turns to a small positive bias with 47R1 and is at times very large during fire events in July–August and December. The positive bias of CY47R1 over North America is much improved with CY47R1_NEWDEP, which shows a nearly null mean bias. The FGE is often improved with CY47R1_NEWDEP compared to CY45R1. This increase in simulated biomass burning aerosols could be caused by changes in deposition, as there are no changes in the GFAS emissions used between the three experiments. It is very likely that the use of injection heights for biomass burning emissions in the two CY47R1 experiments also plays a role. Over Africa, the bias of CY45R1 against AERONET is smaller than over other regions. CY47R1 shows a larger negative bias of 0.05, which is in turn reduced by CY47R1_NEWDEP. Besides other changes, the implementation of the new dust emission scheme probably plays a significant role regarding the changes in the skill scores over Africa. The FGE of simulated AOD at 500 nm is generally improved compared to CY45R1 (more so with CY47R1_NEWDEP) with values generally between 0.4 and 0.5. There is little difference between the two CY47R1 experiments over China; the CY45R1 experiment shows a significant positive bias after August 2017. The bias is generally quite small with the two CY47R1 experiments, and FGE is generally improved (sometimes significantly, such as in summer). For the September–December 2017 period, RMSE (not shown) is nearly halved. Finally, CY45R1 displays a significant negative bias of 0.2 on average over India. This bias is more than halved with the two

CY47R1 experiments. The impact on FGE is generally positive.

6.7 Evaluation against remote sensing products

6.7.1 AOD

In order to assess the relative error of the simulated AOD at 550 nm compared to the merged AOD at 550 nm product from Sogacheva et al. (2020), the fractional gross error (FGE) is used, and thus the errors of the model in simulating relatively low values are not overlooked compared to the larger errors that occur in regions where AOD is usually higher, such as over deserts and biomass burning regions.

Figure 7 shows co-located retrieved and simulated AOD at 550 nm together with the fractional gross error of the simulated AOD. Over most oceans, CY45R1 is generally the closest to the merged AOD product, but the changes in wet and dry deposition of CY47R1_NEWDEP bring a significant increase in simulated AOD compared to CY47R1. The improved skill of the new sea salt aerosol emission schemes shows in the FGE plots, which are significantly improved compared to CY45R1 over most of oceans with CY47R1 (and even more so with CY47R1_NEWDEP). Over most regions, the FGE of CY47R1_NEWDEP is lower than CY47R1. The decrease in FGE between CY45R1 and CY47R1 is not general: it concerns most of Europe, China, Canada, and Russia; a majority of oceans; and the western Sahara. A few areas show a degradation in FGE, i.e. parts of the eastern Sahara, Indonesia and the central Pacific.
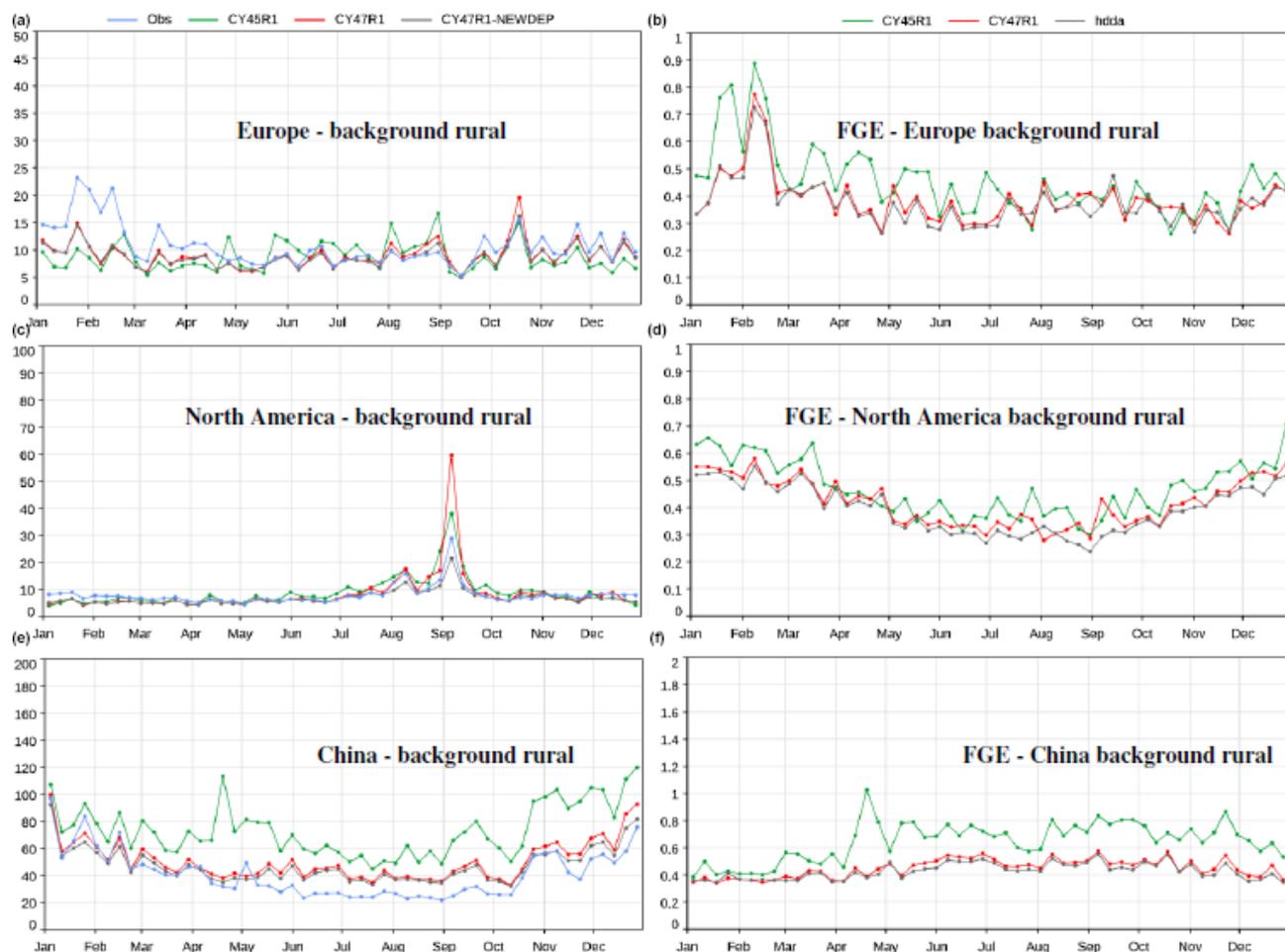
Figure 9. The left column shows observed and simulated weekly PM$_{2.5}$ over Europe (background rural, **a**), North America (background urban, **c**) and China (all sites, **e**). The right column shows the fractional gross error (FGE) of simulated PM$_{2.5}$ against observations.

6.7.2 Dust deposition

Figure 8 shows a comparison of this climatological dust deposition against values simulated by a long-cycle 47R1 cycling forecast (i.e. without data assimilation) experiment, which uses a configuration similar to CY47R1_NEWDUST. Overall, despite a local underestimation of the simulated dust deposition, the retrieved and simulated values match very well, which is a good indicator that IFS-AER manages to capture the climatological deposition of dust relatively well. However, it seems that deposition is overestimated close to the African coastline and underestimated in the western Atlantic, a sign that transatlantic transport of dust is possibly underestimated by IFS-AER.

6.8 Evaluation against PM$_{2.5}$ observations

PM$_{2.5}$ is a key product provided by the global CAMS service. As such, its evaluation is of special importance. Observed PM$_{2.5}$ has been gathered from three geographical areas: Europe, North America and China. Over China, the site

classification (rural or urban and background or traffic) is not known, and thus the statistics probably include many sites that are not really suitable for comparison against simulations by a global model with a relatively coarse horizontal resolution.

Over the background rural stations of Europe, PM$_{2.5}$ simulated by CY45R1 displayed a significant negative bias of 2–5 μg m^{-3} in general, reaching more than 10 μg m^{-3} in January–February 2017. This period of the year 2017 witnessed a severe cold wave across much of Europe, which was probably associated with higher levels of residential wood burning and thus anthropogenic aerosol emissions. This kind of impact of meteorological parameters on emissions is currently not taken into account. The negative bias over Europe by CY45R1 is significantly improved by the two CY47R1 experiments, which simulated PM$_{2.5}$ 2–3 μg m^{-3} higher than CY45R1 in winter months. The negative bias in January and February 2017 is decreased by CY47R1 but far from eliminated. CY47R1_NEWDEP is generally close to CY47R1, except in August and mid-October 2017. The
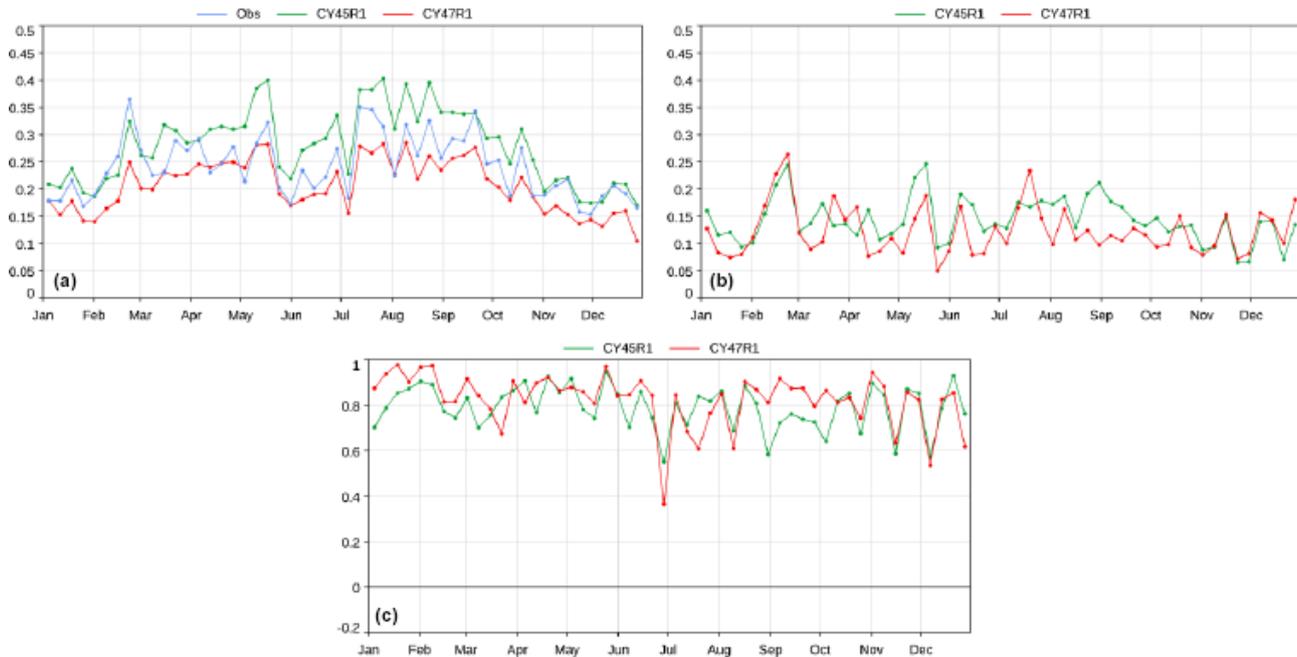
Figure 10. (a) Observed and simulated weekly averaged AOD in 2017 over a selection of 24 AERONET stations more representative of desert conditions. **(b)** RMSE of simulated AOD against AERONET AOD at these 24 stations. **(c)** Spatial correlation between simulated and observed AOD at 500 nm. The AERONET stations used in this plot are: Tizi Ouzou, Tamanrasset INM, Sede Boker, Mezaira, Masdar Institute, Lampedusa, KAUST Campus, Izana, Tunis Carthage, Ilorin, Santa Cruz de Tenerife, La Laguna, Dakar, Dalanzadgad, Cairo EMA, Dushanbe, Arica, Gobabeb, Windpoort, Ben Salem, Cabo Verde, La Parguera, Teide, El Farafra.

mid-October 2017 spike in $PM_{2.5}$ is associated with the large fires that struck Portugal. The RMSE of CY47R1_NEWDEP (not shown) is much lower than CY47R1, which shows that the new deposition options have a beneficial impact on the skill of simulated biomass burning plumes. Generally speaking, the FGE of CY47R1 is significantly better than that of CY45R1, with a decrease of 0.1–0.2 in general. RMSE (not shown) shows a larger relative improvement in summer, when the error is at times more than halved.

The overall picture is slightly different over the background rural stations of North America, where the simulated $PM_{2.5}$ by CY45R1 shows little bias in winter months but a significant positive bias of 2–3 $\mu g\,m^{-3}$ on average during summer months. As in Europe, the simulated $PM_{2.5}$ is generally lowered by 1–2 $\mu g\,m^{-3}$ in general when using the CY47R1 experiments, with even lower values during summer. This results in a small negative bias of 1–2 $\mu g\,m^{-3}$ with CY47R1 from January to April 2017 and a generally small bias in the remaining months. The difference between CY47R1 and CY47R1_NEWDEP is mainly significant during summer, when CY47R1_NEWDEP is generally lower than CY47R1, and this is probably associated with biomass burning aerosols. A spike in simulated $PM_{2.5}$ in early September 2017 with CY47R1 is associated with fire events. The significant positive bias of simulated $PM_{2.5}$ by CY47R1 during this event is much improved by CY47R1_NEWDEP. As already noted over Europe, it seems

that CY47R1_NEWDEP generally improves the skill of the model in simulating PM from fire events. The FGE of simulated $PM_{2.5}$ is, as over Europe, significantly improved by the two CY47R1 experiments for all months.

Over China, CY45R1 overestimates simulated $PM_{2.5}$ constantly and by a large margin from 20 $\mu g\,m^{-3}$ to 40–60 $\mu g\,m^{-3}$ from September to December 2017. On average, the simulated $PM_{2.5}$ is twice as high as the averaged observations. The very high positive bias is significantly reduced by CY47R1, for which the positive bias does not exceed 20 $\mu g\,m^{-3}$, and it is further reduced by 5–10 $\mu g\,m^{-3}$ in the winter months by CY47R1_NEWDEP. The improvement with CY47R1 is largely explained by the improved representation of the sulfur cycle in CY47R1 associated with the coupling to IFS-CB05. In the end, CY47R1_NEWDEP shows little bias from January to April 2017, a significant positive bias of 10–20 $\mu g\,m^{-3}$ from May to October, and a smaller bias for the rest of 2017. Associated with this large improvement in bias is a decrease of FGE with CY47R1 by 0.2–0.4 in CY47R1_NEWDEP. For the whole of 2017, the FGE of CY47R1_NEWDEP is decreased by up to 50 %, and the RMSE (not shown) is around 3 times lower than that over CY45R1. The absolute value is still high, at 30 $\mu g\,m^{-3}$ on average, but this could also reflect the fact that many traffic stations are included in this dataset, for which there is a high representativity error when comparing against global forecasts at a 50 km horizontal resolution.
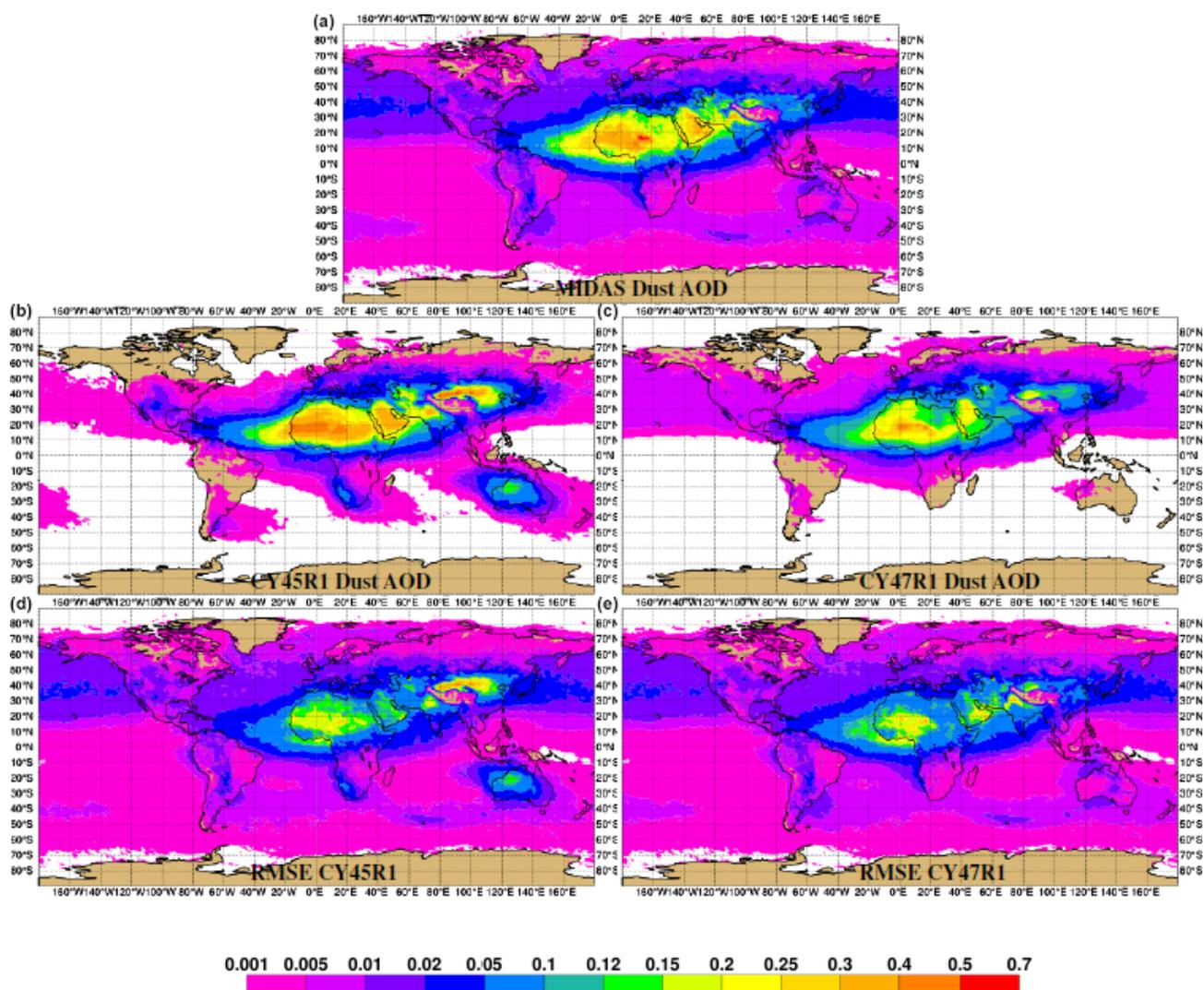
Figure 11. (a) The 2017 average MIDAS dust AOD at 550 nm. Co-located 2017 average of dust AOD at 550 nm simulated by IFS-AER CY45R1 **(b)** and CY47R1 **(c)**. The 2017 average daily RMSE of simulated dust AOD at 550 nm for CY45R1 **(d)** and CY47R1 **(e)**.

6.9 Evaluation of desert dust aspects

In order to evaluate and compare the skills of the two dust emission schemes, the simulated AODs at 500 nm as simulated by 45R1 (which uses the G01 scheme) and 47R1 (which uses the N12 scheme) have been compared against values observed at a selection of AERONET stations that are dominated by dust. Figure 10 shows such a comparison using RMSE instead of fractional gross error (FGE) as a metric of the forecast error because for an evaluation focusing on desert dust, focusing on large simulated values that correspond to extreme events is welcome. Despite higher emissions, the simulated dust AOD is significantly lower on average for the selected stations. A positive bias with the older scheme turns into a small negative bias. The skill of the simulated dust seems to improve with the new scheme, as RMSE is generally decreased and sometimes nearly halved, such as

in August–September 2017 with a value of 0.1 instead of 0.2. The spatial correlation is also generally improved and stands above 0.9 most of the time with CY47R1, whereas it is frequently below this value with CY45R1.

The dust AOD simulated by IFS-AER CY45R1 and CY47R1 has been compared against daily dust AOD at 550 nm provided by the ModIs Dust AeroSol (MIDAS, Gkikas et al., 2020) dataset. Figure 11 shows the retrieved dust AOD at 550 nm averaged over 2017, as well as the co-located average as simulated by IFS-AER CY45R1 and CY47R1. The simulated dust AOD exhibits strong overestimation over the Taklamakan and Gobi region with CY45R1, as well as a less pronounced overestimation over most of the other dust-producing regions. With CY47R1, the simulated values are generally closer, as shown by the reduced averaged RMSE. Over a few areas, such as over the southern part
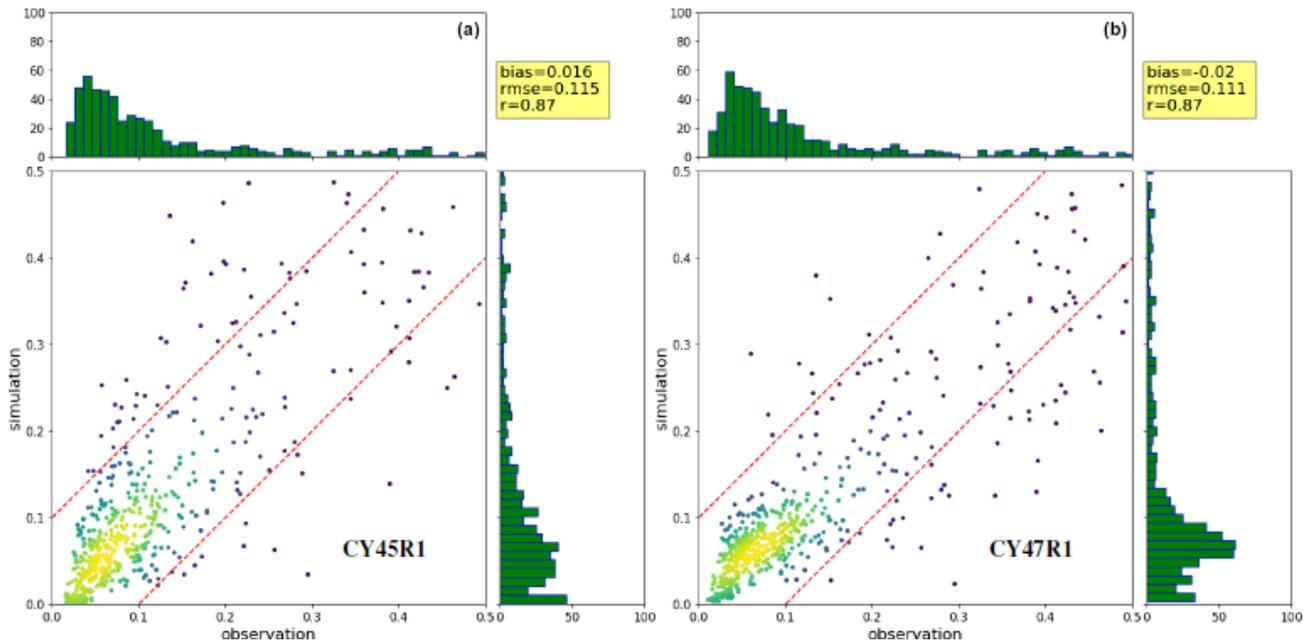
Figure 12. Density scatterplot (for 2017) of AOD at 550 nm simulated by IFS-AER (**a** cycle 45R1, **b** cycle 47R1) and observed by the MAN network.
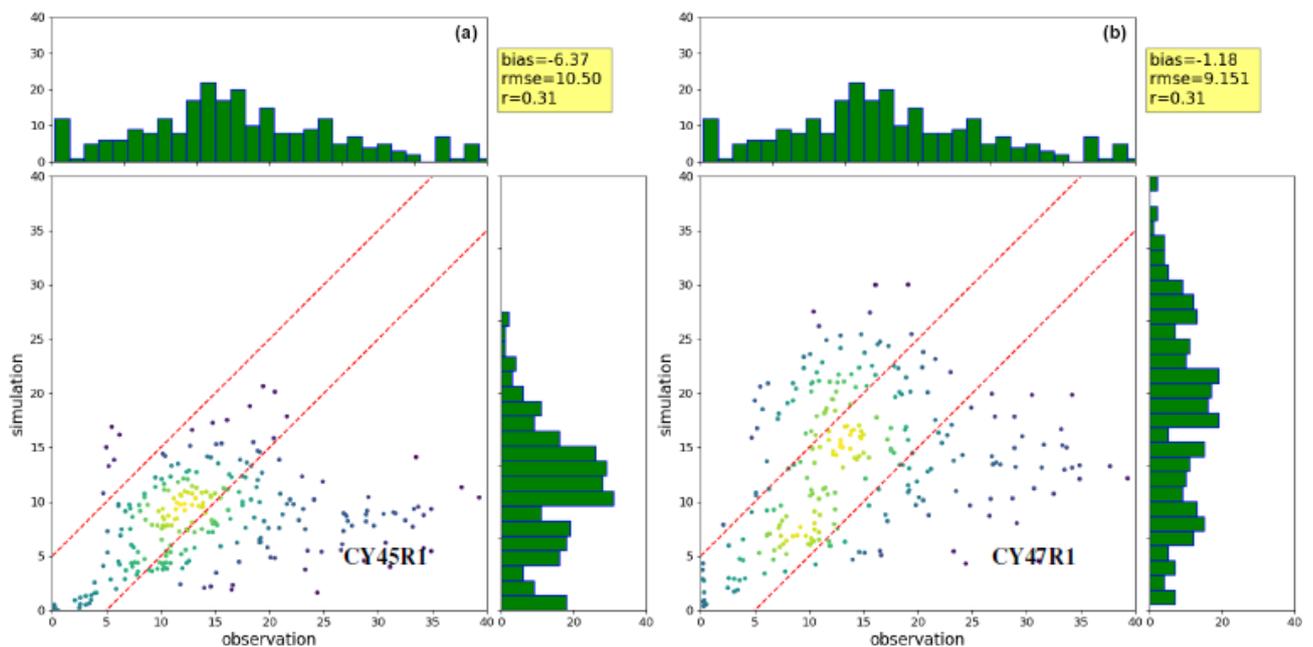

Figure 13. Density plot (for 2017) of monthly simulated (**a** CY45R1, **b** CY47R1) sea salt surface concentration (in µg m^{-3}; sum of bin1 and bin2) vs. climatological values from 21 AEROCE/SEAREX stations.

of the Arabian Peninsula and the Atlantic Ocean, the RMSE is larger with CY47R1.

6.10 Evaluation of sea salt aerosol aspects

An evaluation of the new A16 scheme has been carried out against co-located AOD at 550 nm observations from the

Maritime Aerosol Network (MAN, Smirnov et al. (2009)) against AOD at 550 nm from a selection of 14 AERONET (Holben et al., 1998) stations that are more representative of sea salt aerosols and against climatological monthly sea salt aerosol surface concentration observations from the AERO-CE/SEAREX programme. The AERONET stations used are
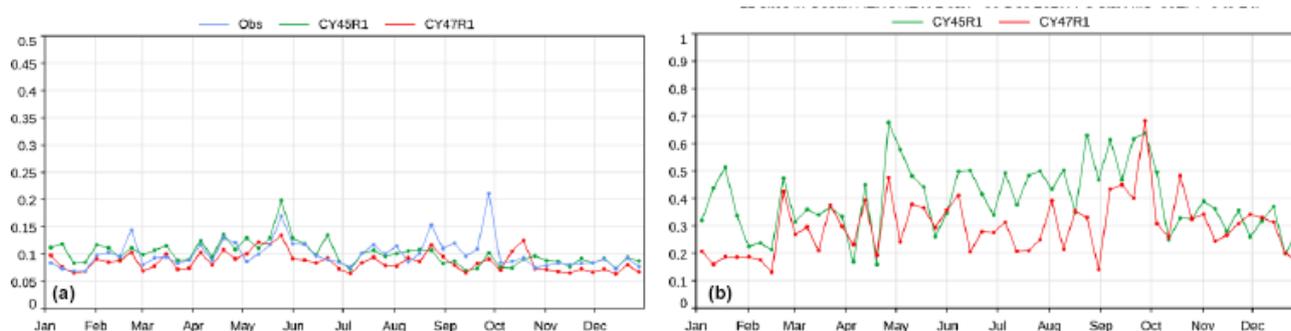
Figure 14. (a) Observed and simulated AOD (averaged weekly) in 2017 over a selection of 14 AERONET stations more representative of sea salt aerosol. **(b)** Fractional gross error (FGE) of simulated AOD against AERONET AOD at these 14 stations.
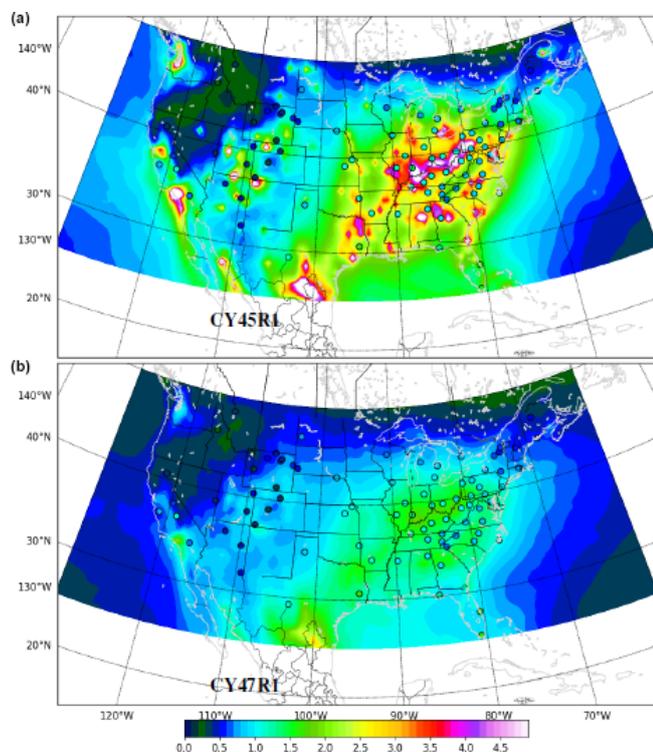
Figure 15. Mean 2017 surface sulfate concentration (in $\mu g\,m^{-3}$) simulated by CY45R1 **(a)** and CY47R1 **(b)** against the yearly average of the CASTNET network (shown as black circles).

Ragged Point, Reunion St Denis, Noumea, Midway Island, Key Biscayne, Key Biscayne2, Cape San Juan, Edinburgh, Cabo da Roca, ARM Graciosa, American Samoa, Amsterdam Island, Andenes and Birkenes. Figure 12 shows the evaluation against total AOD at 550 nm from the MAN network. Total AOD provided by MAN cruises generally (but not always) consists mostly of sea salt aerosol optical depth. Occasionally, dust or biomass burning plumes can also have an impact, but this impacts a minority of the measurements. Figure 12 shows that a small positive bias of 0.016 of simulated AOD at 550 nm against MAN data turns into a small negative

bias of -0.02, with little changes in correlation. The RMSE is slightly improved with CY47R1, decreasing from 0.115 to 0.111.

In order to assess the skill of simulated surface concentration of sea salt aerosol, observations of sea salt aerosol surface concentration carried out in the AEROCE and SEAREX programmes (Savoie et al., 2002) of the 1980s and 1990s are used as monthly climatologies. These observations were carried out by the University of Miami. As detailed in Jaeglé et al. (2011), these observations were carried out in ambient conditions with PM_{10} inlets, which is nearly consistent with the sum of bin1 and bin2 surface concentration (i.e. sea salt aerosols with a radius at 80 % relative humidity of up to 5 μm). Figure 13 shows that a small negative bias of 6.4 $\mu g\,m^{-3}$ with CY45R1 is significantly reduced with CY47R1 and that RMSE is also lowered. The negative bias of CY45R1 may seem inconsistent with the positive bias in simulated AOD against MAN observations, but this apparent inconsistency can be explained by the fact that only the sum of bin1 and bin2 is used in the comparison against AEROCE/SEAREX data, whereas most of the sea salt aerosol emissions and burden in cycle 45R1 concern bin3, as shown in Table 5.

Finally, Fig. 14 compares simulated and observed AOD at 550 nm over a selection of 14 AERONET sites that are more representative of sea salt aerosol. The same remark can be made as for the MAN observations, i.e. that non-sea-salt aerosol probably contributes to some of the observed and simulated values and thus reduces the significance of this evaluation. However, with a careful selection of AERONET sites, it is likely that the contribution of non-sea-salt aerosols is much lower than that of sea salt aerosol. The improvement with CY47R1 is very clear, with a significantly reduced bias and a much improved FGE compared to CY45R1 (0.38 against 0.50), although correlation is low in both cases.
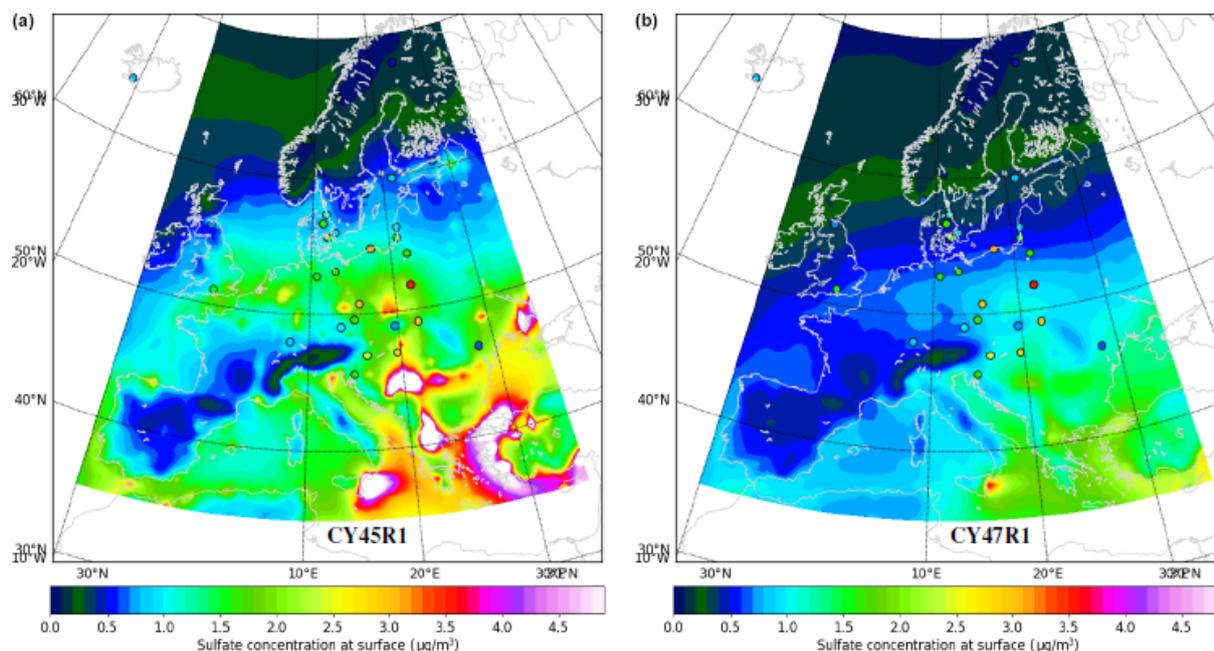
Figure 16. Mean 2017 surface sulfate concentration (in $\mu g\,m^{-3}$) simulated by CY45R1 **(a)** and CY47R1 **(b)** against yearly average from the EMEP network (shown as black circles).

6.11 Evaluation against surface concentration observations

6.11.1 Sulfate

The impact of the coupling of IFS-CB05 and IFS-AER on simulated sulfate surface concentration is significant, as shown by Figs. 15 and 16. CY45R1 is standalone, while CY47R1 runs coupled with IFS-CB05. Over the US, sulfate is much overestimated by standalone IFS-AER at the surface against observations; this positive bias is largely eliminated with coupled IFS-AER. Over Europe, the improvement is less clear, but the trend towards lower simulated sulfate aerosol with CY47R1 at surface is the same.

6.11.2 Nitrate

The sum of the simulated nitrate surface concentration from gas–particle partitioning and from heterogeneous reactions is compared against observations from the CAST-NET and EMEP networks in Fig. 17. In general, nitrate from gas–particle partitioning is simulated over the considered regions to be much more abundant at the surface than nitrate from heterogeneous reactions. The experiment CY47R1_NEWDEP is not shown because the simulated values differ relatively little from those simulated by CY47R1. Over the US, the simulated surface concentration of nitrate is significantly higher than observations. Over much of the eastern US, the simulated values vary between 2 and $4\,\mu g\,m^{-3}$ on average, while the observed values are generally in the range of $1–2\,\mu g\,m^{-3}$. The simulated values are

also significantly overestimated over large parts of Europe, with averages reaching $3–6\,\mu g\,m^{-3}$ against observed values of $3–4\,\mu g\,m^{-3}$ in general. This significant overestimation is a quite frequent feature of global models: it has been noted in GEOS-CHEM (Luo et al., 2019), GFDL (Paulot et al., 2016) and in the Met Office Unified Model (Jones et al., 2021), which has implemented an adapted version of the IFS-AER nitrate scheme. A number of factors can participate to this overestimation: too high particle production compared to the gas phase, which is likely over Europe where the simulated nitric acid surface concentration is much lower than observed; overestimation in the emissions or burden of gaseous precursors of nitric acid; or underestimation of the sinks. Following Paulot et al. (2016), simulations that apply the dry deposition velocity of nitric acid to nitrate have been carried out and were shown to significantly reduce the positive bias of simulated nitrate at surface. However these developments are recent and have not yet been included in operational IFS-AER.

6.11.3 Ammonium

As for nitrate, the simulated surface concentration of ammonium is generally significantly overestimated over the US and Europe, as shown by Fig. 18. This comparison is not exactly representative, as ammonium from ammonium sulfate is part of the reported observations, while the ammonium species include only ammonium from ammonium nitrate. Over Europe, ammonia is also very much overestimated, which is not the case of the US. It is possible, at least over Europe, that the
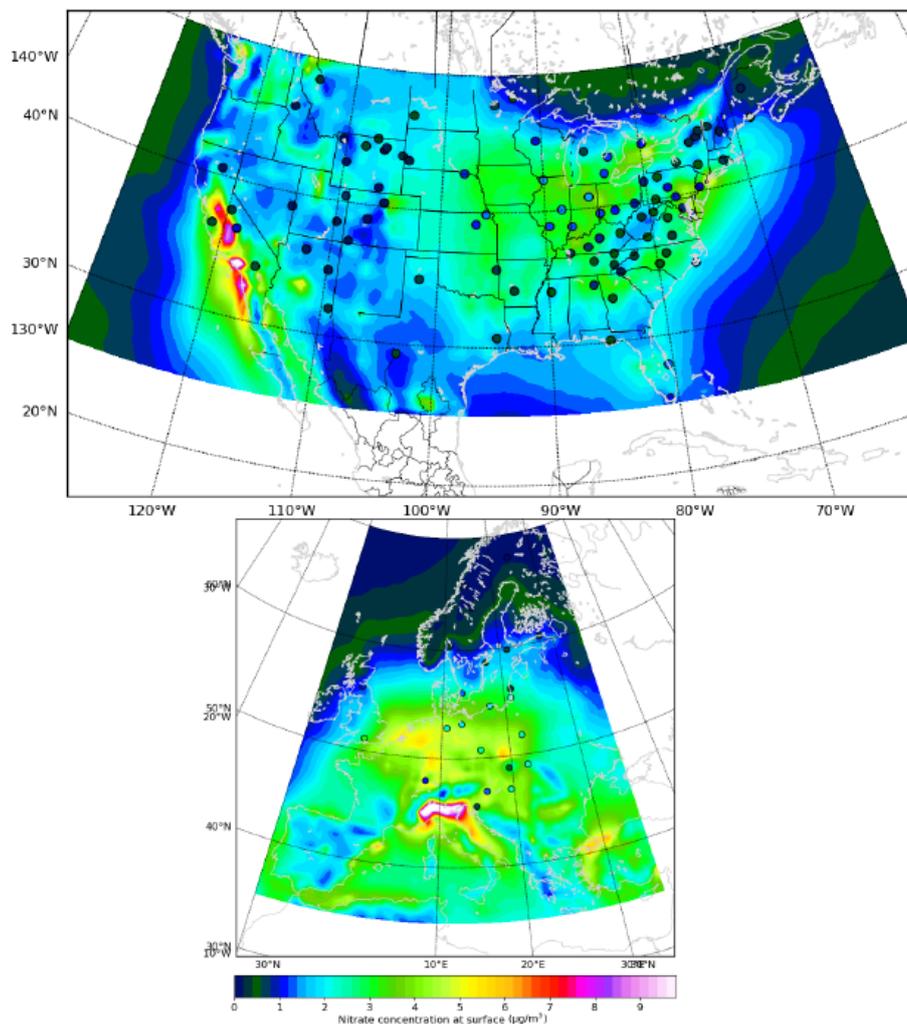
Figure 17. Mean 2017 surface nitrate concentration (in $\mu g\,m^{-3}$) simulated by IFS-AER CY47R1 against yearly average from the CASTNET and the EMEP networks (shown as black circles).

overestimation of ammonium can be partly explained by an ammonia burden that is too high, either from emissions that are too high or there being too little deposition.

6.11.4 Organic carbon

The IMPROVE network disseminates observations of the surface concentration of organic carbon included in $PM_{2.5}$ over the US. Organic carbon has been derived from the hydrophilic and hydrophobic components of simulated organic matter by applying a 2.3 OM : OC ratio for the hydrophilic fraction and a 1.4 ratio for the hydrophobic one. These values are used by the EPA to convert organic matter from CAMS products into organic carbon (Christian Hogrefe, personal communication, 2019). This is a strong assumption, as these ratios are known to vary a lot depending on the aerosol source, transport, ageing, etc. El-Zanan et al. (2005) found a mean value of 2.07 for the OM : OC ratio over all IMPROVE

sites using data from 1988 to 2003, which is consistent with our values. The fraction of organic carbon in $PM_{2.5}$ is derived from the surface concentration of organic carbon by applying a 0.7 factor, consistent with the $PM_{2.5}$ formula used in IFS-AER, which relates to the assumed size distribution of the organic matter species.

Figure 19 shows simulated and observed organic carbon in $PM_{2.5}$ for the three CY45R1, CY47R1 and CY47R1_NEWDEP experiments. The simulated values are very much overestimated with CY45R1, reaching 4–$6\,\mu g\,m^{-3}$ on average in the south-east, while observations are in the range of $2\,\mu g\,m^{-3}$. In the west, spikes of simulated very high values, above $10\,\mu g\,m^{-3}$ correspond to fire events. There are no such spikes in the observed values. The simulated surface concentration of OC in $PM_{2.5}$ is significantly reduced with CY47R1. As the emissions are the same, this can be explained by the use of injection heights for biomass burning emissions and is possibly an impact of the new scaveng-
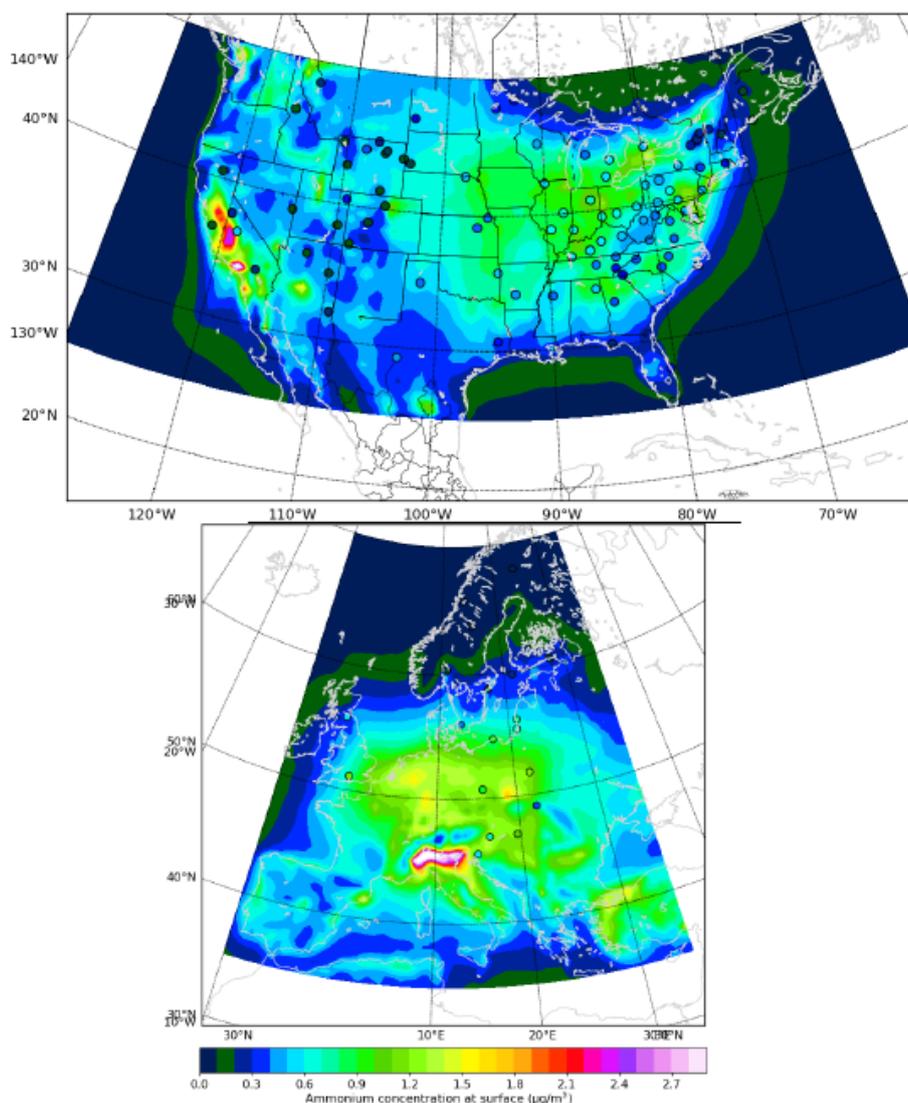
Figure 18. Mean 2017 surface ammonium concentration (in µg m^{-3}) simulated by IFS-AER CY47R1 against yearly average from the CASTNET and the EMEP networks (shown as black circles).

ing scheme. Despite this decrease, the simulated values are still generally higher than the observations, e.g. 3–5 µg m^{-3} in the south-east. The spikes associated with fires are smaller in extent but are still present. These spikes are largely reduced with CY47R1_NEWDEP, which is consistent with the conclusions from the evaluation against PM$_{2.5}$ observations, where a strong impact of the new deposition options on simulated PM$_{2.5}$ from biomass burning origin was noted. CY47R1_NEWDEP bring a further significant decrease in simulated surface organic carbon in PM$_{2.5}$ over the whole of the US. Despite this, the simulated values are still generally higher than the observations. This could be explained by the fact that secondary organic aerosols, which represent a large fraction of the emissions of organic matter, are released at the surface, while in reality they are produced by reactions aloft.

6.12 Evaluation of wet deposition fluxes against CASTNET data

Evaluating and constraining the deposition processes is an indispensable step in the development of IFS-AER and any global aerosol model. There is also a wide interest in the evaluation of sulfur and nitrogen (S and N) deposition fluxes, which are generally dominated by wet deposition. Sulfur dioxide and sulfate aerosols impact the acidity of precipitation (Myhre et al., 2017), while oxidised nitrogen aerosols and gases (NO$_3$, HNO$_3$ and reduced nitrogen aerosols and gases (NH$_4$ and NH$_3$) act as powerful plant and microorganisms nutrients when deposited to terrestrial and aquatic ecosystems. On the other hand, excessive input of nitrogen can lead to eutrophication and loss of ecosystem biodiversity and productivity (Fowler et al., 2015)
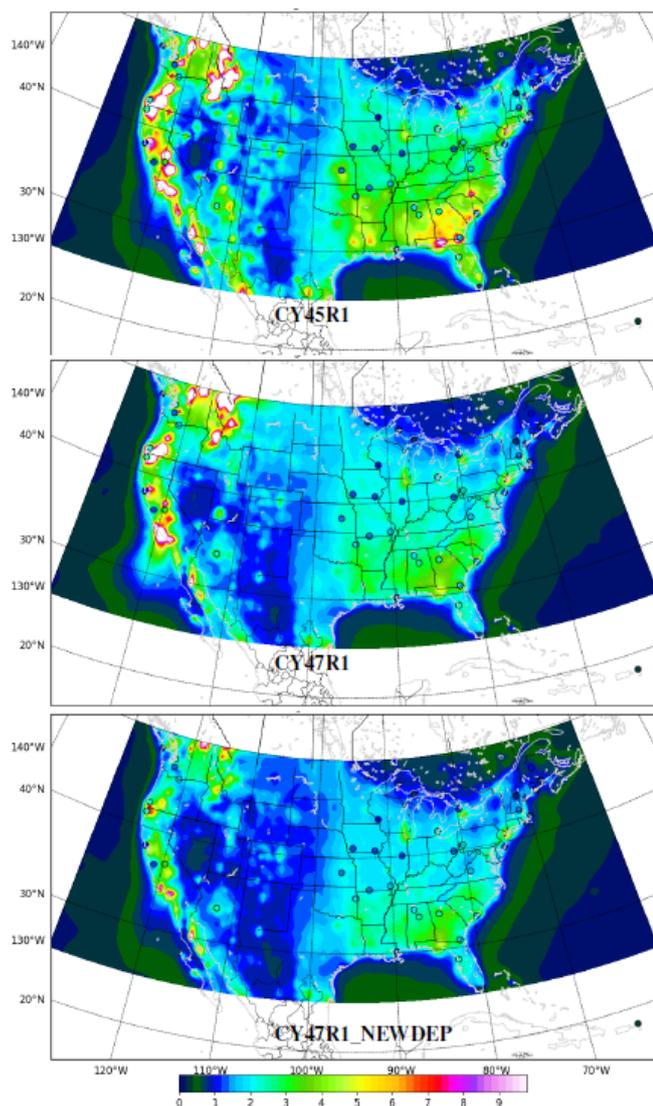
Figure 19. Mean 2017 surface concentration of organic carbon in $PM_{2.5}$ (in $\mu g\,m^{-3}$) simulated by IFS-AER CY47R1 against the yearly average from the IMPROVE network (shown as black circles).

Table 11. Bias, RMSE and spatial correlation factor (R) of simulated yearly sulfur wet deposition fluxes vs. CASTNET observations (in $g\,S\,m^{-2}\,yr^{-1}$).

Experiment	Bias	RMSE	Correlation
CY45R1	0.027	0.065	0.78
CY47R1	0.056	0.085	0.75
CY47R1_NEWDEP	0.046	0.075	0.75

The simulated sulfur wet deposition fluxes for 2017 are shown in Fig. 20. Besides wet deposition, other model changes impacted wet deposition fluxes between cycle 45R1 and 47R1, in particular the changes in sulfate production. The sulfur wet deposition fluxes increased with CY47R1, but this can be caused by changes in wet deposition and/or the presence of a higher sulfate conversion rate. The simulated fluxes are slightly higher compared to values provided by the CASTNET network. The simulated wet deposition derived from the Luo et al. (2019) approach gives slightly lower values compared to the operational wet deposition scheme of CY47R1, which brings the simulated values closer to the observations. Overall, the agreement between the simulated and observed sulfur cycle is good for cycle 47R1 with the wet deposition adapted from Luo et al. (2019), although values can be overestimated over some mountainous areas such as the western and eastern fringes of the Rocky Mountains.

Table 11 presents the aggregated skill scores of the simulated yearly sulfur wet deposition fluxes over the US against CASTNET data. The bias and correlation are degraded by CY47R1 compared to CY45R1; however, this is possibly a case of compensating biases, as the surface concentration of sulfate is simulated much better by CY47R1 compared to CY45R1. The new wet deposition option improves significantly on CY47R1, but it does not reach the values attained for CY45R1.

7 Conclusions

IFS-AER represents a simple modelling approach where many processes are either overlooked or heavily simplified in order to meet the computational cost constraints associated with a global operational production. However, thanks to continuous development and evaluation, as well as drawing on the deeper integration with the global chemistry component of the IFS, the skill of IFS-AER in simulating AOD and PM has been increasing significantly compared to results obtained with cycle CY45R1. The evaluation is more and more diverse, making use of a large amount of ground and remote sensing datasets, which allows for a more detailed diagnostic of the shortcomings of IFS-AER. Despite an improved skill in simulating many aspects and aerosol species, a significant overestimation in simulated nitrate, ammonium and organic carbon at the surface has been noted. In addition,
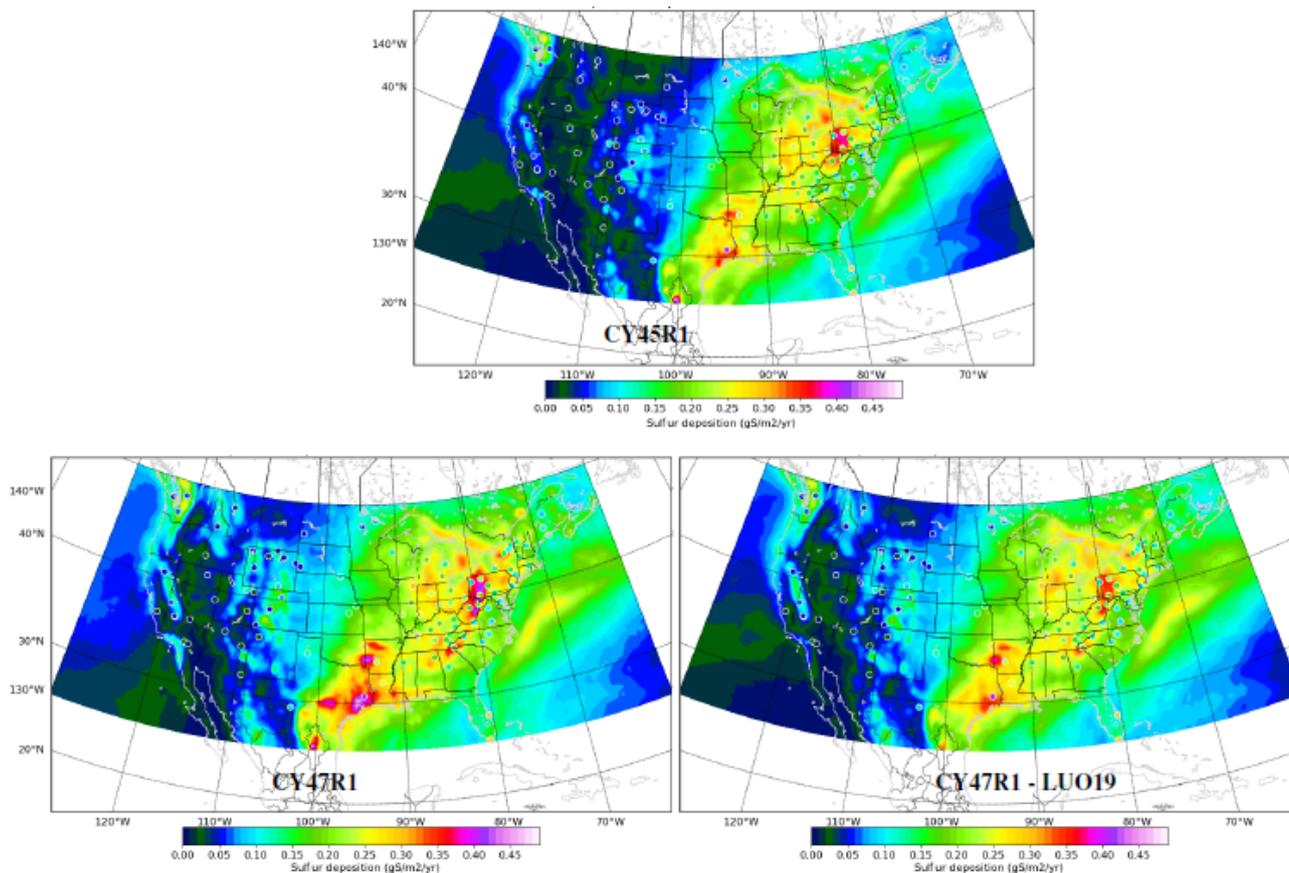
Because of this high impact, S and N deposition fluxes are the subject of numerous studies, particularly within the framework of the Task Force on Hemispheric Transport of Air Pollution (HTAP) of the World Meteorological Organization (Tan et al., 2018; Vet et al., 2014). Regionally over Europe, the Eurodelta Trends model intercomparison exercise also focused on S and N deposition fluxes (Theobald et al., 2019). IFS-AER coupled with IFS-CB05 is well placed to simulate the gaseous and aerosol components of the S and N deposition fluxes. An exhaustive evaluation of simulated S and N deposition fluxes against the global dataset provided by Vet et al. (2014) has been carried out but is out of scope for this paper. Here, we present an evaluation of the simulated S wet deposition flux.

Figure 20. Simulated vs. retrieved wet deposition flux of sulfur over the United States for 2017.

some size distribution assumptions are outdated and need revision. Work is ongoing to address these issues in future operational cycles. This includes the future specific treatment of secondary organic aerosols with the implementation of a new species with anthropogenic and biogenic components and a strong coupling to the global chemistry, which will represent the life cycle of the secondary organic precursors and provide the production rates of secondary organic aerosols. Finally, a more complex gas–particle partitioning scheme, EQSAM4Clim (Metzger et al., 2016), is in the process of being implemented, with the hope of improving the representation of gas–particle partitioning processes in IFS-AER. In the longer term, the implementation of EQSAM4Clim could also help in improving the representation of water uptake and aerosol ageing in IFS-AER.

Author contributions. SR drafted the paper. SR, ZK, VH and JF maintain and carry out developments on IFS-AER. PN and MM contributed to the desert dust and sea salt parameterisations. VH contributed to the coupling with IFS-CB05. MA, RE and VHP contributed to drafting and revising this article.

Disclaimer. Publisher's note: Copernicus Publications remains neutral with regard to jurisdictional claims in published maps and institutional affiliations.

lic the following datasets: NASA (MODIS, AERONET), the European Environment Agency (airbase), the AirNow network and the United States Environmental Protection Agency (EPA for the CASTNET and IMPROVE data), the Finnish Meteorological Institute (FMI, merged AOD product), and the National Observatory of Athens (MIDAS product). We acknowledge the provision of Chinese $PM_{2.5}$ data by Bas Mijling (KNMI) that were acquired as part of the MarcoPolo–Panda project.

Review statement. This paper was edited by Augustin Colette and reviewed by three anonymous referees.

References

Agustí-Panareda, A., Massart, S., Chevallier, F., Boussetta, S., Balsamo, G., Beljaars, A., Ciais, P., Deutscher, N. M., Engelen, R., Jones, L., Kivi, R., Paris, J.-D., Peuch, V.-H., Sherlock, V., Vermeulen, A. T., Wennberg, P. O., and Wunch, D.: Forecasting global atmospheric CO_2, Atmos. Chem. Phys., 14, 11959–11983, https://doi.org/10.5194/acp-14-11959-2014, 2014.

Agusti-Panareda, A., Diamantakis, M., Bayona, V., Klappenbach, F., and Butz, A.: Improving the inter-hemispheric gradient of total column atmospheric CO_2 and CH_4 in simulations with the ECMWF semi-Lagrangian atmospheric global model, Geosci. Model Dev., 10, 1–18, https://doi.org/10.5194/gmd-10-1-2017, 2017.

Albert, M. F. M. A., Anguelova, M. D., Manders, A. M. M., Schaap, M., and de Leeuw, G.: Parameterization of oceanic whitecap fraction based on satellite observations, Atmos. Chem. Phys., 16, 13725–13751, https://doi.org/10.5194/acp-16-13725-2016, 2016.

Anguelova, M. D. and Webster, F.: Whitecap coverage from satellite measurements: A first step toward modeling the variability of oceanic whitecaps, J. Geophys. Res., 111, C03017, https://doi.org/10.1029/2005JC003158, 2006.

Benedetti, A., Morcrette, J.-J., Boucher, O., Dethof, A., Engelen, R., Fisher, M., Flentje, H., Huneeus, N., Jones, L., Kaiser, J., Kinne, S., Mangold, A., Razinger, M., Simmons, A. J., and Suttie, M.: Aerosol analysis and forecast in the European centre for medium-range weather forecasts integrated forecast system: 2. Data assimilation, J. Geophys. Res.-Atmos., 114, D13205, https://doi.org/10.1029/2008JD011115, 2009.

Bian, H., Chin, M., Hauglustaine, D. A., Schulz, M., Myhre, G., Bauer, S. E., Lund, M. T., Karydis, V. A., Kucsera, T. L., Pan, X., Pozzer, A., Skeie, R. B., Steenrod, S. D., Sudo, K., Tsigaridis, K., Tsimpidi, A. P., and Tsyro, S. G.: Investigation of global particulate nitrate from the AeroCom phase III experiment, Atmos. Chem. Phys., 17, 12911–12940, https://doi.org/10.5194/acp-17-12911-2017, 2017.

Boucher, O., Pham, M., and Venkataraman, C.: Simulation of the atmospheric sulfur cycle in the Laboratoire de Meteorologie Dynamique general circulation model: Model description, model evaluation, and global and European budgets, Note Scientifique de l'IPSL, CNRS, 23, 27 pp., 2002.

Bourgeois, Q. and Bey, I.: Pollution transport efficiency toward the Arctic: Sensitivity to aerosol scavenging and source regions, J. Geophys. Res., 116, D08213, https://doi.org/10.1029/2010jd015096, 2011.

Croft, B., Lohmann, U., Martin, R. V., Stier, P., Wurzler, S., Feichter, J., Posselt, R., and Ferrachat, S.: Aerosol size-dependent below-cloud scavenging by rain and snow in the ECHAM5-HAM, Atmos. Chem. Phys., 9, 4653–4675, https://doi.org/10.5194/acp-9-4653-2009, 2009.

de Bruine, M., Krol, M., van Noije, T., Le Sager, P., and Röckmann, T.: The impact of precipitation evaporation on the atmospheric aerosol distribution in EC-Earth v3.2.0, Geosci. Model Dev., 11, 1443–1465, https://doi.org/10.5194/gmd-11-1443-2018, 2018.

Dentener, F., Kinne, S., Bond, T., Boucher, O., Cofala, J., Generoso, S., Ginoux, P., Gong, S., Hoelzemann, J. J., Ito, A., Marelli, L., Penner, J. E., Putaud, J.-P., Textor, C., Schulz, M., van der Werf, G. R., and Wilson, J.: Emissions of primary aerosol and precursor gases in the years 2000 and 1750 prescribed data-sets for AeroCom, Atmos. Chem. Phys., 6, 4321–4344, https://doi.org/10.5194/acp-6-4321-2006, 2006.

Diamantakis, M. and Flemming, J.: Global mass fixer algorithms for conservative tracer transport in the ECMWF model, Geosci. Model Dev., 7, 965–979, https://doi.org/10.5194/gmd-7-965-2014, 2014.

ECMWF: About OpenIFS, https://confluence.ecmwf.int/display/OIFS/About+OpenIFS, last access: 23 June 2022.

El-Zanan, H., Lowenthal, D., Zielinska, B., Chow, J., and Kumar, N.: Determination of the organic aerosol mass to organic carbon ratio in IMPROVE samples, Chemosphere, 60, 485–498, 2005.

Engelen, R. J., Serrar, S., and Chevallier, F.: Four-dimensional data assimilation of atmospheric CO_2 using AIRS observations, J. Geophys. Res.-Atmos., 114, D03303, https://doi.org/10.1029/2008JD010739, 2009.

Fecan, F., Marticorena, B., and Bergametti, G.: Parameterization of the increase of aeolian erosion threshold wind friction velocity due to soil moisture for arid and semi-arid areas, Ann. Geophys., 17, 149–157, https://doi.org/10.1007/s00585-999-0149-7, 1999.

Flemming, J., Inness, A., Flentje, H., Huijnen, V., Moinat, P., Schultz, M. G., and Stein, O.: Coupling global chemistry transport models to ECMWF's integrated forecast system, Geosci. Model Dev., 2, 253–265, https://doi.org/10.5194/gmd-2-253-2009, 2009.

Flemming, J., Huijnen, V., Arteta, J., Bechtold, P., Beljaars, A., Blechschmidt, A.-M., Diamantakis, M., Engelen, R. J., Gaudel, A., Inness, A., Jones, L., Josse, B., Katragkou, E., Marecal, V., Peuch, V.-H., Richter, A., Schultz, M. G., Stein, O., and Tsikerdekis, A.: Tropospheric chemistry in the Integrated Forecasting System of ECMWF, Geosci. Model Dev., 8, 975–1003, https://doi.org/10.5194/gmd-8-975-2015, 2015.

Fowler, D., Steadman, C. E., Stevenson, D., Coyle, M., Rees, R. M., Skiba, U. M., Sutton, M. A., Cape, J. N., Dore, A. J., Vieno, M., Simpson, D., Zaehle, S., Stocker, B. D., Rinaldi, M., Facchini, M. C., Flechard, C. R., Nemitz, E., Twigg, M., Erisman, J. W., Butterbach-Bahl, K., and Galloway, J. N.: Effects of global change during the 21st century on the nitrogen cycle, Atmos. Chem. Phys., 15, 13849–13893, https://doi.org/10.5194/acp-15-13849-2015, 2015.

Gelaro, R., McCarty, W., Suárez, M. J., Todling, R., Molod, A., Takacs, L., Randles, C. A., Darmenov, A., Bosilovich, M. G., Reichle, R., Wargan, K., Coy, L., Cullather, R., Draper, C., Akella, S., Buchard, V., Conaty, A., da Silva, A. M., Gu, W., Kim, G.,

Koster, R., Lucchesi, R., Merkova, D., Nielsen, J. E., Partyka, G., Pawson, S., Putman, W., Rienecker, M., Schubert, S. D., Sienkiewicz, M., and Zhao, B.: The Modern-Era Retrospective Analysis for Research and Applications, Version 2 (MERRA-2), J. Climate, 30, 5419–5454, https://doi.org/10.1175/JCLI-D-16-0758.1, 2017.

Gilette, D. A.: Environmental Factors Affecting Dust Emission by Wind Erosion, in: Saharan Dust, edited by: Morales, C., Scope 14, John Wiley & Sons, New York, 71–91, 1979.

Ginoux, P., Chin, M., Tegen, I., Prospero, J. M., Holben, B., Dubovik, O., and Lin, S.-J.: Sources and distributions of dust aerosols simulated with the GOCART model, J. Geophys. Res.-Atmos., 106, 20255–20273, 2001.

Ginoux, P., Prospero, J. M., Gill, T. E., Hsu, N. C., and Zhao, M.: Global-scale attribution of anthropogenic and natural dust sources and their emission rates based on MODIS Deep Blue aerosol products, Rev. Geophys., 50, RG3005, https://doi.org/10.1029/2012RG000388, 2012.

Giorgi, F. and Chameides, W. L.: Rainout lifetimes of highly soluble aerosols and gases as inferred from simulations with a general circulation model, J. Geophys. Res., 91, 367–376, 1986.

Gkikas, A., Proestakis, E., Amiridis, V., Kazadzis, S., Di Tomaso, E., Tsekeri, A., Marinou, E., Hatzianastassiou, N., and Pérez García-Pando, C.: ModIs Dust AeroSol (MIDAS): a global fine-resolution dust optical depth data set, Atmos. Meas. Tech., 14, 309–334, https://doi.org/10.5194/amt-14-309-2021, 2021.

Gliß, J., Mortier, A., Schulz, M., Andrews, E., Balkanski, Y., Bauer, S. E., Benedictow, A. M. K., Bian, H., Checa-Garcia, R., Chin, M., Ginoux, P., Griesfeller, J. J., Heckel, A., Kipling, Z., Kirkevåg, A., Kokkola, H., Laj, P., Le Sager, P., Lund, M. T., Lund Myhre, C., Matsui, H., Myhre, G., Neubauer, D., van Noije, T., North, P., Olivié, D. J. L., Rémy, S., Sogacheva, L., Takemura, T., Tsigaridis, K., and Tsyro, S. G.: AeroCom phase III multi-model evaluation of the aerosol life cycle and optical properties using ground- and space-based remote sensing as well as surface in situ observations, Atmos. Chem. Phys., 21, 87–128, https://doi.org/10.5194/acp-21-87-2021, 2021.

Granier, C., Bessagnet, B., Bond, T., D'Angiola, A., van der Gon, H. D., Frost, G. J., Heil, A., Kaiser, J. W., Kinne, S., Klimont, Z., Kloster, S., Lamarque, J.-F., Liousse, C., Masui, T., Meleux, F., Mieville, A., Ohara, T., Raut, J.-C., Riahi, K., Schultz, M. G., Smith, S. J., Thomson, A., van Aardenne, J., van der Werf, G. R., and van Vuuren, D. P.: Evolution of anthropogenic and biomass burning emissions of air pollutants at global and regional scales during the 1980–2010 period, Climate Change, 109, 163–190, 2011.

Granier, C., Darras, S., Denier van der Gon, H., Doubalova, J., Elguindi, N., Galle, B., Gauss, M., Guevara, M., Jalkanen, J.-P., Kuenen, J., Liousse, C., Quack, B., Simpson, D., and Sindelarova, K.: The Copernicus Atmosphere Monitoring Service global and regional emissions (April 2019 version), CAMS reports, https://doi.org/10.24380/d0bn-kx16, 2019.

Grythe, H., Ström, J., Krejci, R., Quinn, P., and Stohl, A.: A review of sea-spray aerosol source functions using a large global set of sea salt aerosol concentration measurements, Atmos. Chem. Phys., 14, 1277–1297, https://doi.org/10.5194/acp-14-1277-2014, 2014.

Hauglustaine, D. A., Balkanski, Y., and Schulz, M.: A global model simulation of present and future nitrate aerosols and their direct radiative forcing of climate, Atmos. Chem. Phys., 14, 11031–11063, https://doi.org/10.5194/acp-14-11031-2014, 2014.

Holben, B. N., Eck, T., Slutsker, I., Tanre, D., Buis, J., Setzer, A., Vermote, E., Reagan, J., Kaufman, Y., Nakajima, T., Holben, B. N., Eck, T. F., Slutsker, I., Tanré, D., Buis, J. P., Setzer, A., Vermote, E., Reagan, J. A., Kaufman, Y. J., Nakajima, T., Lavenu, F., Jankowiak, I., and Smirnov, A.: AERONET–A federated instrument network and data archive for aerosol characterization, Remote Sens. Environ., 66, 1–16, 1998.

Hollingsworth, A., Engelen, R. J., Textor, C., Benedetti, A., Boucher, O., Chevallier, F., Dethof, A., Elbern, H., Eskes, H., Flemming, J., Granier, C., Kaiser, J. W., Morcrette, J.-J., Rayner, P., Peuch, V. H., Rouil, L., Schultz, M. G., Simmons, A. J., and Consortium, T. G.: Toward a Monitoring and Forecasting System For Atmospheric Composition: The GEMS Project, B. Am. Meteorol. Soc., 89, 1147–1164, 2008.

Hortal, M.: The development and testing of a new two-time-level semi-Lagrangian scheme (SETTLS) in the ECMWF forecast model, Q. J. Roy. Meteor. Soc., 128, 1671–1687, 2002.

Huijnen, V., Williams, J., van Weele, M., van Noije, T., Krol, M., Dentener, F., Segers, A., Houweling, S., Peters, W., de Laat, J., Boersma, F., Bergamaschi, P., van Velthoven, P., Le Sager, P., Eskes, H., Alkemade, F., Scheele, R., Nédélec, P., and Pätz, H.-W.: The global chemistry transport model TM5: description and evaluation of the tropospheric chemistry version 3.0, Geosci. Model Dev., 3, 445–473, https://doi.org/10.5194/gmd-3-445-2010, 2010.

Huijnen, V., Flemming, J., Chabrillat, S., Errera, Q., Christophe, Y., Blechschmidt, A.-M., Richter, A., and Eskes, H.: C-IFS-CB05-BASCOE: stratospheric chemistry in the Integrated Forecasting System of ECMWF, Geosci. Model Dev., 9, 3071–3091, https://doi.org/10.5194/gmd-9-3071-2016, 2016.

Huijnen, V., Le Sager, P., Köhler, M. O., Carver, G., Rémy, S., Flemming, J., Chabrillat, S., Errera, Q., and van Noije, T.: OpenIFS/AC: atmospheric chemistry and aerosol in OpenIFS 43r3, Geosci. Model Dev. Discuss. [preprint], https://doi.org/10.5194/gmd-2022-80, in review, 2022.

Inness, A., Baier, F., Benedetti, A., Bouarar, I., Chabrillat, S., Clark, H., Clerbaux, C., Coheur, P., Engelen, R. J., Errera, Q., Flemming, J., George, M., Granier, C., Hadji-Lazaro, J., Huijnen, V., Hurtmans, D., Jones, L., Kaiser, J. W., Kapsomenakis, J., Lefever, K., Leitão, J., Razinger, M., Richter, A., Schultz, M. G., Simmons, A. J., Suttie, M., Stein, O., Thépaut, J.-N., Thouret, V., Vrekoussis, M., Zerefos, C., and the MACC team: The MACC reanalysis: an 8 yr data set of atmospheric composition, Atmos. Chem. Phys., 13, 4073–4109, https://doi.org/10.5194/acp-13-4073-2013, 2013.

Inness, A., Ades, M., Agustí-Panareda, A., Barré, J., Benedictow, A., Blechschmidt, A.-M., Dominguez, J. J., Engelen, R., Eskes, H., Flemming, J., Huijnen, V., Jones, L., Kipling, Z., Massart, S., Parrington, M., Peuch, V.-H., Razinger, M., Remy, S., Schulz, M., and Suttie, M.: The CAMS reanalysis of atmospheric composition, Atmos. Chem. Phys., 19, 3515–3556, https://doi.org/10.5194/acp-19-3515-2019, 2019.

Jaeglé, L., Quinn, P. K., Bates, T. S., Alexander, B., and Lin, J.-T.: Global distribution of sea salt aerosols: new constraints from in situ and remote sensing observations, Atmos. Chem. Phys., 11, 3137–3157, https://doi.org/10.5194/acp-11-3137-2011, 2011.

Jones, A. C., Hill, A., Remy, S., Abraham, N. L., Dalvi, M., Hardacre, C., Hewitt, A. J., Johnson, B., Mulcahy, J. P., and Turnock, S. T.: Exploring the sensitivity of atmospheric nitrate concentrations to nitric acid uptake rate using the Met Office's Unified Model, Atmos. Chem. Phys., 21, 15901–15927, https://doi.org/10.5194/acp-21-15901-2021, 2021.

Khan, T. R. and Perlinger, J. A.: Evaluation of five dry particle deposition parameterizations for incorporation into atmospheric transport models, Geosci. Model Dev., 10, 3861–3888, https://doi.org/10.5194/gmd-10-3861-2017, 2017.

Kok, J. F.: A scaling theory for the size distribution of emitted dust aerosols suggests climate models underestimate the size of the global dust cycle, P. Natl. Acad. Sci. USA, 108, 1016–1021, 2011.

Levy, R. C., Mattoo, S., Munchak, L. A., Remer, L. A., Sayer, A. M., Patadia, F., and Hsu, N. C.: The Collection 6 MODIS aerosol products over land and ocean, Atmos. Meas. Tech., 6, 2989–3034, https://doi.org/10.5194/amt-6-2989-2013, 2013.

Luo, G., Yu, F., and Schwab, J.: Revised treatment of wet scavenging processes dramatically improves GEOS-Chem 12.0.0 simulations of surface nitric acid, nitrate, and ammonium over the United States, Geosci. Model Dev., 12, 3439–3447, https://doi.org/10.5194/gmd-12-3439-2019, 2019.

Mahowald, N., Albani, S., Kok, J. F., Engelstaeder, S., Scanza, R., Ward, D., and Flanner, M.: The size distribution of desert dust aerosols and its impacts on the Earth system, Aeolian Res., 15, 53–71, https://doi.org/10.1016/j.aeolia.2013.09.002, 2014.

Marticorena, B. and Bergametti, G.: Modeling the atmosphere dust cycle: 1. Design of a soil-derived dust emission scheme, J. Geophys. Res., 100, 16415–16430, 1995.

Metzger, S., Dentener, F., Pandis, S., and Lelieveld, J.: Gas/aerosol partitioning: 1. A computationally efficient model, J. Geophys. Res., 107, 4312, https://doi.org/10.1029/2001JD001102, 2002.

Metzger, S., Steil, B., Abdelkader, M., Klingmüller, K., Xu, L., Penner, J. E., Fountoukis, C., Nenes, A., and Lelieveld, J.: Aerosol water parameterisation: a single parameter framework, Atmos. Chem. Phys., 16, 7213–7237, https://doi.org/10.5194/acp-16-7213-2016, 2016.

Michou, M., Nabat, P., and Saint-Martin, D.: Development and basic evaluation of a prognostic aerosol scheme (v1) in the CNRM Climate Model CNRM-CM6, Geosci. Model Dev., 8, 501–531, https://doi.org/10.5194/gmd-8-501-2015, 2015.

Monahan, E. C. and Muircheartaigh, I. O.: Optimal power-law description of oceanic whitecap coverage dependence on wind speed, J. Phys. Oceanogr., 10, 2094–2099, 1980.

Monahan, E. C., Spiel, D. E., and Davidson, K. L.: A model of marine aerosol generation via whitecaps and wave disruption, in: Oceanic Whitecaps and Their Role in Air–Sea Exchange Processes, edited by: Monahan, E. C., MacNiocaill, G., and Reidel, D., Springer, 167–174, 1986.

Morcrette, J.-J., Boucher, O., Jones, L., Salmond, D., Bechtold, P., Beljaars, A., Benedetti, A., Bonet, A., Kaiser, J., Razinger, M., Morcrette, J.-J., Boucher, O., Jones, L., Salmond, D., Bechtold, P., Beljaars, A., Benedetti, A., Bonet, A., Kaiser, J. W., Razinger, M., Schulz, M., Serrar, S., Simmons, A. J., Sofiev, M., Suttie, M., Tompkins, A. M., and Untch, A.: Aerosol analysis and forecast in the European Centre for medium-range weather forecasts integrated forecast system: Forward modeling, J. Geophys. Res.-

Atmos., 114, D06206, https://doi.org/10.1029/2008JD011235, 2009.

Myhre, G., Aas, W., Cherian, R., Collins, W., Faluvegi, G., Flanner, M., Forster, P., Hodnebrog, Ø., Klimont, Z., Lund, M. T., Mülmenstädt, J., Lund Myhre, C., Olivié, D., Prather, M., Quaas, J., Samset, B. H., Schnell, J. L., Schulz, M., Shindell, D., Skeie, R. B., Takemura, T., and Tsyro, S.: Multi-model simulations of aerosol and ozone radiative forcing due to anthropogenic emission changes during the period 1990–2015, Atmos. Chem. Phys., 17, 2709–2720, https://doi.org/10.5194/acp-17-2709-2017, 2017.

Nabat, P., Solmon, F., Mallet, M., Kok, J. F., and Somot, S.: Dust emission size distribution impact on aerosol budget and radiative forcing over the Mediterranean region: a regional climate model approach, Atmos. Chem. Phys., 12, 10545–10567, https://doi.org/10.5194/acp-12-10545-2012, 2012.

Paulot, F., Ginoux, P., Cooke, W. F., Donner, L. J., Fan, S., Lin, M.-Y., Mao, J., Naik, V., and Horowitz, L. W.: Sensitivity of nitrate aerosols to ammonia emissions and to nitrate chemistry: implications for present and future nitrate optical depth, Atmos. Chem. Phys., 16, 1459–1477, https://doi.org/10.5194/acp-16-1459-2016, 2016.

Popp, T., De Leeuw, G., Bingen, C., Brühl, C., Capelle, V., Chedin, A., Clarisse, L., Dubovik, O., Grainger, R., Griesfeller, J., Heckel, A., Kinne, S., Klüser, L., Kosmale, M., Kolmonen, P., Lelli, L., Litvinov, P., Mei, L., North, P., Pinnock, S., Povey, A., Robert, C., Schulz, M., Sogacheva, L., Stebel, K., Stein Zweers, D., Thomas, G., Tilstra, L. G., Vandenbussche, S., Veefkind, P., Vountas, M., and Xue, Y.: Development, Production and Evaluation of Aerosol Climate Data Records from European Satellite Observations (Aerosol_cci), Remote Sens.-Basel, 8, 421, https://doi.org/10.3390/rs8050421, 2016.

Reddy, M. S., Boucher, O., Bellouin, N., Schulz, M., Balkanski, Y., Dufresne, J.-L., and Pham, M.: Estimates of global multicomponent aerosol optical depth and direct radiative perturbation in the Laboratoire de Météorologie Dynamique general circulation model, J. Geophys. Res., 110, D10S16, https://doi.org/10.1029/2004JD004757, 2005.

Rémy, S. and Anguelova, M.: Improving the Representation of Whitecap Fraction and Sea Salt Aerosol Emissions in the ECMWF IFS-AER, Remote Sens.-Basel, 13, 4856, https://doi.org/10.3390/rs13234856, 2021.

Rémy, S., Veira, A., Paugam, R., Sofiev, M., Kaiser, J. W., Marenco, F., Burton, S. P., Benedetti, A., Engelen, R. J., Ferrare, R., and Hair, J. W.: Two global data sets of daily fire emission injection heights since 2003, Atmos. Chem. Phys., 17, 2921–2942, https://doi.org/10.5194/acp-17-2921-2017, 2017.

Rémy, S., Kipling, Z., Flemming, J., Boucher, O., Nabat, P., Michou, M., Bozzo, A., Ades, M., Huijnen, V., Benedetti, A., Engelen, R., Peuch, V.-H., and Morcrette, J.-J.: Description and evaluation of the tropospheric aerosol scheme in the European Centre for Medium-Range Weather Forecasts (ECMWF) Integrated Forecasting System (IFS-AER, cycle 45R1), Geosci. Model Dev., 12, 4627–4659, https://doi.org/10.5194/gmd-12-4627-2019, 2019.

Savoie, D. L., Arimoto, R., Keene, W. C., Prospero, J. M., Duce, R. A., and Galloway, J. N.: Marine biogenic and anthropogenic contributions to non-sea-salt sulfate in the marine boundary layer

over the North Atlantic Ocean, J. Geophys. Res.-Atmos., 107, 4356, https://doi.org/10.1029/2001JD000970, 2002.

Shangguan, W., Dai, Y., Duan, Q., Liu, B., and Yuan, H.: A global soil data set for earth system modeling, J. Adv. Model. Earth Sy., 6, 249–263, 2014.

Smirnov, A., Holben, B., Slutsker, I., Giles, D., McClain, S., Eck, T., Sakerin, S., Macke, A., Croot, P., Zibordi, G., Quinn, P., Sciare, J., Kinne, S., Harvey, M., Smyth, T., Piketh, S., Zielinski, G., Proshutinsky, A., Goes, J. I., Nelson, N. B., Larouche, P., Radionov, V. F., Goloub, P., Krishna Moorthy, K., Matarrese, R., Robertson, E., and Jourdin, F.: Maritime Aerosol Network as a component of Aerosol Robotic Network, J. Geophys. Res., 114, D06204, https://doi.org/10.1029/2008JD011257, 2009.

Sogacheva, L., Popp, T., Sayer, A. M., Dubovik, O., Garay, M. J., Heckel, A., Hsu, N. C., Jethva, H., Kahn, R. A., Kolmonen, P., Kosmale, M., de Leeuw, G., Levy, R. C., Litvinov, P., Lyapustin, A., North, P., Torres, O., and Arola, A.: Merging regional and global aerosol optical depth records from major available satellite products, Atmos. Chem. Phys., 20, 2031–2056, https://doi.org/10.5194/acp-20-2031-2020, 2020.

Spracklen, D. V., Jimenez, J. L., Carslaw, K. S., Worsnop, D. R., Evans, M. J., Mann, G. W., Zhang, Q., Canagaratna, M. R., Allan, J., Coe, H., McFiggans, G., Rap, A., and Forster, P.: Aerosol mass spectrometer constraint on the global secondary organic aerosol budget, Atmos. Chem. Phys., 11, 12109–12136, https://doi.org/10.5194/acp-11-12109-2011, 2011.

Stier, P., Feichter, J., Kinne, S., Kloster, S., Vignati, E., Wilson, J., Ganzeveld, L., Tegen, I., Werner, M., Balkanski, Y., Schulz, M., Boucher, O., Minikin, A., and Petzold, A.: The aerosol-climate model ECHAM5-HAM, Atmos. Chem. Phys., 5, 1125–1156, https://doi.org/10.5194/acp-5-1125-2005, 2005.

Tan, J., Fu, J. S., Dentener, F., Sun, J., Emmons, L., Tilmes, S., Sudo, K., Flemming, J., Jonson, J. E., Gravel, S., Bian, H., Davila, Y., Henze, D. K., Lund, M. T., Kucsera, T., Takemura, T., and Keating, T.: Multi-model study of HTAP II on sulfur and nitrogen deposition, Atmos. Chem. Phys., 18, 6847–6866, https://doi.org/10.5194/acp-18-6847-2018, 2018.

Theobald, M. R., Vivanco, M. G., Aas, W., Andersson, C., Ciarelli, G., Couvidat, F., Cuvelier, K., Manders, A., Mircea, M., Pay, M.-T., Tsyro, S., Adani, M., Bergström, R., Bessagnet, B., Briganti, G., Cappelletti, A., D'Isidoro, M., Fagerli, H., Mar, K., Otero, N., Raffort, V., Roustan, Y., Schaap, M., Wind, P., and Colette, A.: An evaluation of European nitrogen and sulfur wet deposition and their trends estimated by six chemistry transport models for the period 1990–2010, Atmos. Chem. Phys., 19, 379–405, https://doi.org/10.5194/acp-19-379-2019, 2019.

Vet, R., Artz, R. S., Carou, S., Shaw, M., Ro, C. U., Aas, W., Baker, A., Bowersox, V. C., Dentener, F., Galy-Lacaux, C., Hou, A., Pienaar, J. J., Gillett, R., Forti, M. C., Gromov, S., Hara, H., Khodzher, T., Mahowald, N. M., Nickovic, S., Rao, P. S. P., and Reid, N. W.: A global assessment of precipitation chemistry and deposition of sulfur, nitrogen, sea salt, base cations, organic acids, acidity and pH, and phosphorus, Atmos. Environ., 93, 3–100, https://doi.org/10.1016/j.atmosenv.2013.10.060, 2014.

Vincent, J., Laurent, B., Losno, R., Bon Nguyen, E., Roullet, P., Sauvage, S., Chevaillier, S., Coddeville, P., Ouboulmane, N., di Sarra, A. G., Tovar-Sánchez, A., Sferlazzo, D., Massanet, A., Triquet, S., Morales Baquero, R., Fornier, M., Coursier, C., Desboeufs, K., Dulac, F., and Bergametti, G.: Variability of mineral dust deposition in the western Mediterranean basin and south-east of France, Atmos. Chem. Phys., 16, 8749–8766, https://doi.org/10.5194/acp-16-8749-2016, 2016.

Waza, A., Schneiders, K., May, J., Rodríguez, S., Epple, B., and Kandler, K.: Field comparison of dry deposition samplers for collection of atmospheric mineral dust: results from single-particle characterization, Atmos. Meas. Tech., 12, 6647–6665, https://doi.org/10.5194/amt-12-6647-2019, 2019.

Yarwood, G., Rao, S., Yocke, M., and Whitten, G.: Updates to the carbon bond chemical mechanism: CB05, Final report to the US EPA, EPA Report Number: RT-0400675, http://www.camx.com (last access: 3 April 2019), 2005.

Yu, H., Tan, Q., Chin, M., Remer, L. A., Kahn, R. A., Bian, H., Dongchul, K., Zhibo, Z., Tianle, Y., Ali, O., Winker, D., Levy, R., Kalashnikova, O., Crepeau, L., Capelle, V., and Chédin, A.: Estimates of African dust deposition along the trans-Atlantic transit using the decadelong record of aerosol measurements from CALIOP, MODIS, MISR, and IASI, J. Geophys. Res., 124, 7975–7996, 2019.

Zender, C. S., Newman, D., and Torres, O.: Spatial heterogeneity in aeolian erodibility: Uniform, topographic, geomorphic, and hydrologic hypotheses, J. Geophys. Res., 108, 4543–4555, 2003.

Zhang, L. and He, Z.: Technical Note: An empirical algorithm estimating dry deposition velocity of fine, coarse and giant particles, Atmos. Chem. Phys., 14, 3729–3737, https://doi.org/10.5194/acp-14-3729-2014, 2014.

Zhang, L., Gong, S., Padro, J., and Barrie, L.: A size-segregated particle dry deposition scheme for an atmospheric aerosol module, Atmos. Environ., 35, 549–560, https://doi.org/10.1016/S1352-2310(00)00326-5, 2001.